3D printed energy harvesters for railway bridges-Design optimisation

J.C. Cámara-Molina [a], E. Moliner [b], M.D. Martínez-Rodrigo [b], D.P. Connolly [c], D. Yurchenko [d], P. Galvín [a,e], A. Romero [a,*]

[a] *Escuela Técnica Superior de Ingeniería, Universidad de Sevilla, Camino de los Descubrimientos s/n, ES 41092 Sevilla, Spain*
[b] *Universitat Jaume I, Department of Mechanical Engineering and Construction, Avda. Sos Baynat s/n, ES 12071 Castellón, Spain*
[c] *Institute for High Speed Rail and Systems Integration, School of Civil Engineering, University of Leeds, UK*
[d] *Institute of Sound and Vibration Research, University of Southampton, Southampton SO17 1BJ, UK*
[e] *ENGREEN, Laboratory of Engineering for Energy and Environmental Sustainability, Universidad de Sevilla, Camino de los Descubrimientos s/n, ES 41092 Sevilla, Spain*

ARTICLE INFO

ABSTRACT

This paper investigates the optimal design of 3D printed energy harvesters for railway bridges. The type of harvester studied is a cantilever bimorph beam with a mass at the tip and a load resistance. These parameters are adjusted to find the optimal design that tunes the harvester to the fundamental frequency of the bridge. An analytical model based on a variational formulation to represent the electromechanical behaviour of the device is presented. The optimisation problem is solved using a genetic algorithm with constraints of geometry and structural integrity. The proposed procedure is implemented in the design and manufacture of an energy harvesting device for a railway bridge on an in-service high-speed line. To do so, first the methodology is validated experimentally under laboratory conditions and shown to offer strong performance. Next the in-situ railway bridge is instrumented using accelerometers and the results used to evaluate energy harvesting performance. The results show the energy harvested in a time window of three and a half hours (20 train passages) is $E = 109.32$ mJ. The proposed methodology is particularly useful for bridges with fundamental mode shapes above 4.5 Hz, however optimal design curves are also presented for the most common railway bridges found in practice. A novelty of this work is the use of additive manufacturing to 3D print energy harvesters, thus maximising design flexibility and energy performance.

1. Introduction

The rail industry is moving increasingly towards the autonomous and real-time monitoring of infrastructure assets. Remote and distributed detection systems are often used to perform this task [1–3]. However, one of the limiting factors in the implementation of sensor networks in railway structures is the lack of a long-term and low-maintenance power supply. Most existing systems require battery changes, and lack of access and maintenance operations can limit their practical implementation. In this sense, energy harvesting is becoming an alternative to the electrical supply of sensors and nodes in remote areas [4,5]. Piezoelectric energy harvesting systems are an increasingly widespread source of energy that can overcome the uncertainty in some applications, such as photovoltaic energy systems which are affected by climatic factors. Many research efforts are devoted to the development of energy

harvesters based on the piezoelectric effect (PZT) to transform vibrations from the structure where they are installed into electrical energy to be used in small power devices and sensors.

The most common typology is that of a bimorph cantilever beam, which consists of two PZT patches bonded to a substructure. These systems have the ability to generate energy from environmental vibrations in a frequency range of 3–100 Hz [6]. The predominant frequencies of vibrations caused by rail traffic in the infrastructure are within the above range, making it possible to supply low-power devices and sensors. Therefore, research on energy harvesting has been carried out on road bridges [7], railway bridges [8], and track superstructures [9–11], providing an average power of 0.03 mW with an output voltage between 1.8 and 3.6 V. The authors of these works conclude that the energy harvested could be used to power the sensor nodes of monitoring systems. Cahill et al. [12] investigated the feasibility of energy harvesting from train-induced vibration in bridges and its application in Structural Health Monitoring. The power extracted from train passages was less than one milliwatt. Khan and Ahmad [13] studied and developed a piezoelectric vibration energy harvester to power autonomous monitoring systems. In this case, the maximum output power was 7700 μW in the frequency range 1–120 Hz. Song [14] studied the application of energy harvesting in railway bridges and found the root-mean-squared value of the output voltage varied in the range 0.7–5.9 V without a tip mass. The voltage increased to 2.8–205.5 V using a tip mass of 12 g.

An challenge of energy harvesting systems is the narrow efficient frequency band around the resonant frequency [15]. The amount of energy generated is highly dependent on the frequency content of the base excitation since the performance of the device is constrained to a narrow band near its resonant frequency. The output power reduces rapidly if the excitation frequency deviates from the resonant condition when the generator is not sufficiently tuned. However, compared to some applications, the energy harvesting of railway bridges is less sensitive to frequency effects, because the dynamic behaviour of the structure is mainly determined by the fundamental mode shape [16], which is relatively constant. Moreover, the bridge response is mostly due to the quasi-static component of the load, and the influence of dynamic wheel-rail interaction effects is minimal [17]. Thus, the natural frequency of the harvester should be tuned to the fundamental frequency of the bridge [18].

The resonant frequency of a bimorph cantilever beam depends on the stiffness and mass of the system. Tuning is done mainly by adjusting the length and thickness of the substructure and the mass of the tip. These parameters affect the output power that can be obtained. Stephen [19] demonstrated that the output power depends on the excitation frequency, reaching the optimum when the frequency matches the undamped natural frequency of the device. Richards et al. [20] analysed the power conversion efficiency, relating the electromechanical coupling coefficient, the mechanical quality factor, and the power performance for piezoelectric oscillators. The quality factor defines the loss in mechanical conversion and is inversely related to the damping ratio. The authors found that power generation improved by decreasing the stiffness and damping and increasing the mass. Furthermore, Xu and Tang [21] investigated the effect of stiffness compensation by a magnetic field on energy conversion efficiency. The experimental results showed that the electromechanical coupling coefficient can be increased by 65% with 44.1% stiffness compensation.

This work aims at the optimal design of energy harvesting devices on railway bridges. The design parameters are the geometry of the substructure and the mass at the tip, which define the equivalent mass and stiffness of the system, as mentioned above. Although device tuning to the fundamental frequency of the bridge can be done by adjusting the mass and stiffness, the identification of the optimal design point is not straightforward as the electromechanical behaviour depends on the properties of the PZT patch, the substructure, and the mass at the tip. Different optimisation procedures have been proposed to enhance the device performance. Sarker et al. [6] reviewed the application of optimisation algorithms to enhance the performance of piezoelectric energy harvesting systems. Genetic algorithm [22–24], particle swarm optimisation algorithm [25], backtracking search algorithm [26], lightning search algorithm [27] and Kriging aided optimisation [28] have been used to optimise both the PZT and the substructure geometry of cantilever unimorph and bimorph beams. Then, the optimisation algorithms can be used to find the optimal length, width, and thickness of the structure to increase the performance.High-level device optimisation approach was recently proposed in [29] where the authors used surrogate optimisation to improve the power output of a multi-beam structure.

The solution to the optimisation problem leads to a variety in geometry that would require flexible prototyping and manufacturing to practical implementation. In this work, additive manufacturing for the substructure has been chosen instead of typical metal machining manufacturing. 3D printing has become an alternative in many manufacturing sectors of industry, allowing low-cost high-fidelity geometries from CAD models [30], and has been successfully applied in the development of electronic devices [31], in the design of piezoelectric materials [31,32], and in some applications of energy harvesting for ultrasonic devices [33,34] and wearable electronics [35].

The main novelties and most valuable contributions of the present work are the optimal design of energy harvesting devices in railway bridges, including formulation, analytical verification, and experimental validation. The novelties of this contribution when compared to previous one are various. First, an analytical model based on three parameters is proposed to represent the electromechanical behaviour of the system. The proposed model is derived from a variational formulation using a parametric approach based on a dimensionless shape function. This procedure allows for the determination of explicit expressions for the properties of the coupled lumped model (the equivalent and effective mass, the stiffness, and the electromechanical coupling coefficient) which are advantageous to carry out the optimisation problem since the computational cost is much lower than numerical models. The optimisation problem considers only two design variables relating the system mass and stiffness, and is solved using a genetic algorithm with constraints on the geometry and structural integrity. The influence of the load resistance on the optimal design of the harvester is considered by complex modal analysis to estimate the resonant frequency of the system. Second, the proposed procedure is experimentally validated under laboratory conditions. The harvester substructure is manufactured using 3D printing to give the flexibility to maximise the design compatibility with the optimal tuning procedure. The PLA material is selected for the substructure due to the ease of printing and good mechanical properties. In addition, PLA is a sustainable and biodegradable
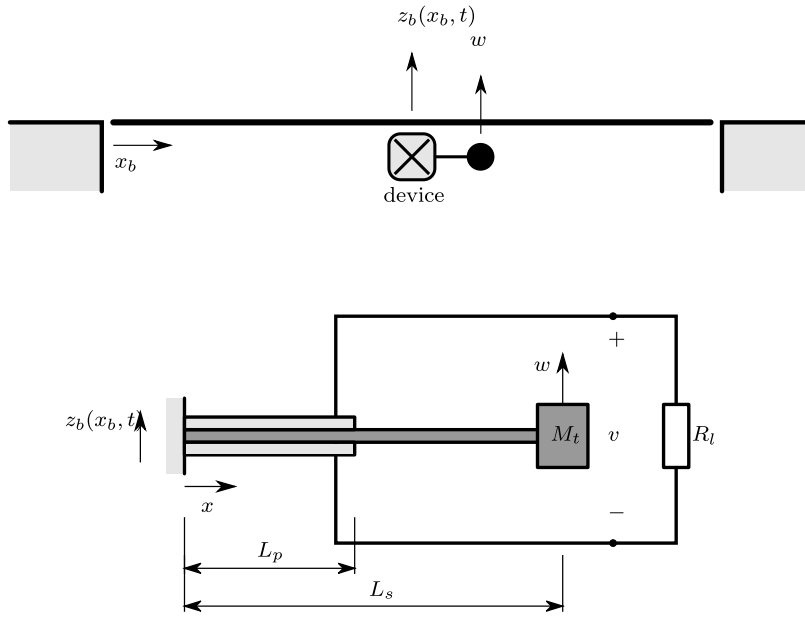
Fig. 1. Scheme of bridge/harvester system.

material with low environmental impact. The structural damping ratio plays an important role in the optimal design because the maximum acceleration is determined by this value and, therefore, the maximum stress in the substructure, which is one of the constraints in the optimisation problem. The damping ratio is experimentally estimated from a non-linear regression model based on the Levenberg–Marquardt least squares algorithm [36]. Finally, the capability of the proposed procedure is demonstrated in the design and manufacturing of an energy harvesting device for a railway bridge from the Madrid–Sevilla High-Speed line.

This paper is divided into the following parts: Section 2 is concerned with the governing equations and the optimal tuning procedure; the proposed approach is later verified in Section 3; and the design, manufacturing, and experimental testing are described in detail in Section 4. Finally, Section 5 presents optimal design curves for most bridges in railway lines with fundamental frequencies prescribed by Eurocode 1 (EC1) [37].

2. Formulation and analysis approach

The proposed approach considers an energy harvesting device attached to the bridge in a section defined by the coordinate x_b (see Fig. 1). This device is subjected to the vertical vibration of the bridge $z_b(x_b, t)$ induced by railway traffic. A strategy based on a coupled piezoelectric-mechanical model is proposed to represent the dynamic behaviour of the device.

A bimorph cantilever beam based on the Euler–Bernoulli beam assumption with a tip mass M_t (Fig. 1) is considered to model the harvester. The system consists of two perfectly attached piezoelectric plates to the substructure. The piezoelectrics are polarised in opposite directions along the thickness of the plate and connected in series. The system feeds a load resistance R_l. The dimensions of the beam are length L_s, width b_s, and thickness h_s, while the dimensions of the piezoelectric plate are length L_p, width b_p and thickness h_p. The properties of the structure material are defined by Young's modulus E_s and the mass density ρ_s.

The bimorph beam has two different sections: (i) the part with piezoelectric patches given by the longitudinal coordinate $x \leq L_p$; and (ii) the substructure without PZT defined by $L_p \leq x \leq L_s$. The following dimensionless parameters relate the geometry, mass, and bending stiffness of both parts:

$$\beta = \frac{L_p}{L_s}, \qquad \gamma = \frac{\overline{EI}}{E_s I_s}, \qquad \mu = \frac{\overline{m}}{\rho_s h_s b_s} \tag{1}$$

where $E_s I_s$ and $\rho_s h_s b_s$ are the bending stiffness and mass per unit length of the substructure; and $\overline{EI}$ and $\overline{m}$ are the equivalent bending stiffness and mass per unit length of the beam section with PZT. Hence, β, γ and μ relate the length, bending stiffness, and mass per unit length of the section with PZT to the substructure, respectively, and are bounded to $\beta \leq 1$, $\gamma > 1$ and $\mu > 1$.

The constitutive equations of the PZT are [38]:

$$\begin{Bmatrix} \mathbf{T} \\ \mathbf{D} \end{Bmatrix} = \begin{bmatrix} \mathbf{c}^E & \mathbf{e} \\ \mathbf{e}^T & -\epsilon^S \end{bmatrix} \begin{Bmatrix} \mathbf{S} \\ -\mathbf{E} \end{Bmatrix} \tag{2}$$

where $\mathbf{T}$ is the stress vector, $\mathbf{D}$ is the electric flux density vector, $\mathbf{S}$ is the elastic strain vector, $\mathbf{E}$ is the electric field intensity vector, $\mathbf{c}^E$ is the compliance matrix evaluated in a constant electric field, $\mathbf{e}$ is the piezoelectric material coupling matrix that relates charge density and strain, and ϵ^S is the absolute permittivity in constant strain.

According to the Euler–Bernoulli assumptions, the shear deformation and rotary inertia of the bimorph beam may be neglected. The vertical displacement of the tip mass w only produces longitudinal stress in the polarised PZT patches in the transverse direction 3, and therefore the device operates in the 31 mode. Then, Eqs. (2) can be reduced to the following:

$$T_1(x, z, t) = c_{11}^E S_1(x, z, t) - e_{31} E_3(x, z, t) \tag{3}$$

$$D_3(x, z, t) = e_{31} S_1(x, z, t) + \epsilon_{33}^S E_3(x, z, t) \tag{4}$$

where the elastic stiffness component c_{11}^E represents the Young's modulus of the PZT, e_{31} is the piezoelectric stress constant, ϵ_{33}^T is the permittivity at constant strain, z is the vertical coordinate of the beam section, and t stands for the time.

The coupled electromechanical behaviour of the bimorph beam is described by the governing equations (3) and (4). The voltage in the series connection of each piezoelectric patch is $v(t)/2$, and the intensity of the electric field is:

$$E_3(t) = -\frac{v(t)}{2h_p} \tag{5}$$

In the previous equation, it is assumed that the electric field does not depend on the longitudinal coordinate x to represent the conductive electrodes of the patch, which fully cover both faces of the PZT patches and are thin enough to neglect their contribution to the bending stiffness.

Furthermore, the axial deformation in the piezoelectric patch S_1 is due to bending and is defined proportionally to the curvature according to the Euler–Bernoulli assumption:

$$S_1(x, z, t) = -z \frac{\partial^2 w(x, t)}{\partial x^2} \tag{6}$$

The equilibrium equation of the cantilever beam subjected to base excitation is [39]:

$$\frac{\partial^2 M(x, t)}{\partial x^2} + m(x) \frac{\partial^2 w(x, t)}{\partial t^2} = -\left[m(x) + M_t \delta(x - L_s) \right] \frac{\partial^2 w(x, t)}{\partial t^2} \tag{7}$$

where $\delta(x)$ is the Dirac delta function and $m(x)$ represents the mass per unit length of the beam. The mass per unit length is $m(x) = \rho_s h_s b_s$ ($L_p \leq x \leq L_s$), while the mass of the beam section with PZT is defined by the parameter μ according to Eq. (1) as $m(x) = \mu \rho_s h_s b_s$ ($0 \leq x \leq L_p$). The mass M_t is assumed to be a point mass. The effect of viscous damping has been omitted in the equilibrium equation for simplicity; and will be later introduced in the governing equation in the following section.

The bending moment of the beam section with PZT is given by:

$$M(x, t) = -b_p \left[\int_{-h_s/2-hp}^{-h_s/2} z T_1(x, z, t)\, dz + \int_{-h_s/2}^{h_s/2} z \sigma_x(x, z, t)\, dz + \int_{h_s/2}^{h_s/2+hp} z T_1(x, z, t)\, dz \right], \qquad 0 \leq x \leq L_p \tag{8}$$

where σ_x represents the longitudinal stress in the substructure ($\sigma_x = E_s \varepsilon_x = -z E_s \partial^2 w / \partial x^2$). The previous expression is further elaborated according to Eqs. (3), (5) and (6):

$$
\begin{aligned}
M(x, t) = b_p & \left[\int_{-h_s/2-hp}^{-h_s/2} \left(z^2 c_{11}^E \frac{\partial^2 w(x, t)}{\partial x^2} - z e_{31} \frac{v(t)}{2h_p} \right) dz + \int_{-h_s/2}^{h_s/2} z^2 E_s \frac{\partial^2 w(x, t)}{\partial x^2}\, dz \right. \\
& \left. + \int_{h_s/2}^{h_s/2+hp} \left(z^2 c_{11}^E \frac{\partial^2 w(x, t)}{\partial x^2} - z e_{31} \frac{v(t)}{2h_p} \right) dz \right], \qquad 0 \leq x \leq L_p
\end{aligned}
\tag{9}
$$

Thus, the bending moment is obtained after integration:

$$M(x, t) = \gamma E_s I_s \frac{\partial^2 w(x, t)}{\partial x^2} - e_{31} h_{pc} b_p v(t), \qquad 0 \leq x \leq L_p \tag{10}$$

where $h_{pc} = (h_p + h_s)/2$ is the distance from the neutral axis of the beam to the centre line of the piezoelectric patch. The parameter γ relates the bending stiffness of the beam section with the PZT, to the bending stiffness of the substructure:

$$\gamma = 1 + \frac{2 n h_p \left(4 h_p^2 + 6 h_p h_s + 3 h_s^2 \right)}{h_s^3} \tag{11}$$

where $n = c_{11}^E / E_s$ relates the Young's modulus of the PZT and the substructure.

The bending moment of the substructure is $M(x, t) = E_s I_s \partial^2 w(x, t) / \partial x^2$, $\quad L_p \leq x \leq L_s$.

2.1. Governing equations

The equation of motion of the bimorph beam is derived from Hamilton's principle, expressing the kinetic energy E_k, the potential energy E_p, and the virtual work δW performed by the base excitation in terms of the generalised coordinate $q(t)$. The beam deflection is approximated by:

$$w(x, t) = q(t) \psi(x) \tag{12}$$

where the generalised coordinate $q(t)$ represents the tip displacement and $\psi(x)$ is a dimensionless shape function that satisfies the boundary conditions. Then, the Lagrange equation of motion is written as follows:

$$\frac{d}{dt}\left(\frac{\partial E_k}{\partial \dot{q}}\right) - \frac{\partial E_k}{\partial q} + \frac{\partial E_p}{\partial q} = Q \tag{13}$$

where the virtual work is expressed as $\delta W = Q\delta q$.

The dimensionless shape function $\psi(x)$ can be estimated from the static equilibrium (Eq. (7)) of the beam under a unit tip load:

$$\gamma E_s I_s \frac{\partial^2 \psi(x)}{\partial x^2} + (x - L_s) = 0 \quad 0 \leq x \leq L_p \tag{14}$$

$$E_s I_s \frac{\partial^2 \psi(x)}{\partial x^2} + (x - L_s) = 0 \quad L_p \leq x \leq L_s \tag{15}$$

The integration of the previous equations is performed by imposing a clamped condition at the fixed end and compatibility of displacement and rotation at $x = L_p$. Once the previous expressions are integrated, the shape function $\psi(x)$ is normalised to unit amplitude. Explicit expressions for the shape function can be found in Appendix.

The constitutive equations (3) and (4) expressed in the generalised coordinates are obtained by combining Eqs. (6) and (12):

$$T_1(x, z, t) = -c_{11}^E z \frac{\partial^2 \psi(x)}{\partial x^2} q(t) + \frac{e_{31}}{2h_p} v(t) \tag{16}$$

$$D_3(x, z, t) = -e_{31} z \frac{\partial^2 \psi(x)}{\partial x^2} q(t) - \frac{\epsilon_{33}^S}{2h_p} v(t) \tag{17}$$

Similarly, the longitudinal deformation in the substructure becomes $\varepsilon_x = -zq\partial^2\psi/\partial x^2$.

Thus, the kinetic energy due to the excitation of the beam and the tip mass is:

$$\begin{aligned}
E_k &= \frac{1}{2}\left[\int_0^{L_p} m(x)\left(\frac{\partial w(x,t)}{\partial t}\right)^2 dx + \int_{L_p}^{L_s} m(x)\left(\frac{\partial w(x,t)}{\partial t}\right)^2 dx + M_t\left(\frac{\partial w(x,t)}{\partial t}\Big|_{x=L_s}\right)^2\right] \\
&= \frac{1}{2}\left[\int_0^{L_p} \mu\rho_s h_s b_s \psi(x)^2 dx + \int_{L_p}^{L_s} \rho_s h_s b_s \psi(x)^2 dx + M_t\right]\dot{q}(t)^2
\end{aligned} \tag{18}$$

The potential energy is calculated from the longitudinal stress T_1 in the PZT patches (Ω_p), the longitudinal stress σ_x in the substructure (Ω_s) and the related piezoelectric and mechanical strains, S_1 and ε_x, respectively:

$$\begin{aligned}
E_p &= \frac{1}{2}\left[\iint_{\Omega_p} T_1(x,z,t)S_1(x,z,t)\,d\Omega + \int_{\Omega_s} \sigma_x(x,z,t)\varepsilon_x(x,z,t)\,d\Omega\right] \\
&= \frac{1}{2}\left[\iint_{\Omega_p} c_{11}^E z^2\left(\frac{\partial^2\psi(x)}{\partial x^2}\right)^2 d\Omega + \int_{\Omega_s} E_s z^2\left(\frac{\partial^2\psi(x)}{\partial x^2}\right)^2 d\Omega\right]q(t)^2 - \frac{1}{2}\left[\iint_{\Omega_p} \frac{e_{31}v(t)}{2h_p}z\left(\frac{\partial^2\psi(x)}{\partial x^2}\right)d\Omega\right]q(t) \\
&= \frac{1}{2}\left[\int_0^{L_p} \gamma E_s I_s\left(\frac{\partial^2\psi(x)}{\partial x^2}\right)^2 dx + \int_{L_p}^{L_s} E_s I_s\left(\frac{\partial^2\psi(x)}{\partial x^2}\right)^2 dx\right]q(t)^2 - \frac{1}{2}\left[\int_0^{L_p} e_{31}b_p h_{pc} v(t)\left(\frac{\partial^2\psi(x)}{\partial x^2}\right)dx\right]q(t)
\end{aligned} \tag{19}$$

The virtual work of the external forces $\delta W_{ext} = Q\delta q$ is:

$$\begin{aligned}
\delta W_{ext} &= -\int_0^{L_p} m(x)\ddot{z}(x_b,t)w(x,t)\,dx - \int_{L_p}^{L_s} m(x)\ddot{z}(x_b,t)w(x,t) - M_t\ddot{z}(x_b,t)w(L_s,t) \\
&= -\left[\int_0^{L_p} \mu\rho_s h_s b_s \ddot{z}(x_b,t)\psi(x)\,dx + \int_{L_p}^{L_s} \rho_s h_s b_s \ddot{z}(x_b,t)\psi(x)\,dx + M_t\right]\delta q(t)
\end{aligned} \tag{20}$$

where Q is expressed in terms of effective mass as $Q = -M_{eff}\ddot{z}(x_b,t)$.

Finally, the Lagrange equation of motion (Eq. (13)) becomes:

$$M_{eq}\ddot{q}(t) + K_{eq}q(t) - \alpha v(t) = -M_{eff}\ddot{z}_b(x_b,t) \tag{21}$$

where the equivalent mass and stiffness, M_{eq} and K_{eq}, and the electromechanical coupling coefficient α are given by:

$$M_{eq} = \int_0^{L_p} \mu\rho_s h_s b_s \psi(x)^2 dx + \int_{L_p}^{L_s} \rho_s h_s b_s \psi(x)^2 dx + M_t \tag{22}$$

$$M_{eff} = \int_0^{L_p} \mu\rho_s h_s b_s \psi(x)\,dx + \int_{L_p}^{L_s} \rho_s h_s b_s \psi(x)\,dx + M_t \tag{23}$$

$$K_{eq} = \int_0^{L_p} \gamma E_s I_s\left(\frac{\partial^2\psi(x)}{\partial x^2}\right)^2 dx + \int_{L_p}^{L_s} E_s I_s\left(\frac{\partial^2\psi(x)}{\partial x^2}\right)^2 dx \tag{24}$$

$$\alpha = \int_0^{L_p} e_{31}b_p h_{pc}\left(\frac{\partial^2\psi(x)}{\partial x^2}\right)dx \tag{25}$$
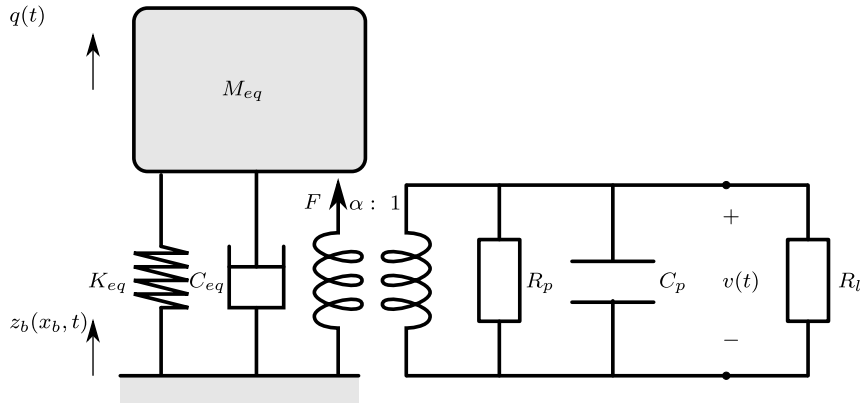
Fig. 2. Lumped-parameter model of a piezoelectric energy harvester.

The explicit expressions of the equivalent mass, the equivalent stiffness, and the electromechanical coupling coefficient are also provided in Appendix.

The coupled electromechanical governing equation is obtained according to Eq. (17) by applying Kirchhoff's laws to the system represented in Fig. 1. The electrical current at the load resistance is given by:

$$
\begin{aligned}
i(t) = \frac{v(t)}{R_l} &= \frac{d}{dt}\left[\iint_{A_p} D_3(x,z,t)\,dA\right] = -\frac{d}{dt}\left[\int_0^{L_p}\left(b_p e_{31} h_{pc}\frac{\partial^2\psi(x)}{\partial x^2}q(t)+\frac{\epsilon_{33}^S b_p v(t)}{2h_p}\right)dx\right]\\
&= -\int_0^{L_p}\left(e_{31}b_p h_{pc}\frac{\partial^2\psi(x)}{\partial x^2}\right)dx\,\dot q(t) - \frac{\epsilon_{33}^S b_p L_p}{2h_p}\dot v(t)
\end{aligned}
\tag{26}
$$

This equation is rewritten as follows:

$$
C_p \dot v(t) + \frac{v(t)}{R_l} + \alpha \dot q(t) = 0
\tag{27}
$$

where the internal electrical capacitance C_p for the series connection is defined as:

$$
C_p = \frac{\epsilon_{33}^S b_p L_p}{2h_p}
\tag{28}
$$

Finally, the governing equations of the coupled lumped model are obtained from Eqs. (21) and (27):

$$
\ddot q(t) + 2\zeta\omega\dot q(t) + \omega^2 q(t) - \frac{\alpha}{M_{eq}}v(t) = -\frac{M_{eff}}{M_{eq}}\ddot z_b
\tag{29}
$$

$$
C_p \dot v(t) + \frac{v(t)}{R_l} + \alpha \dot q(t) = 0
\tag{30}
$$

where v is the output voltage, ζ represents the mechanical damping ratio, $\omega = \sqrt{K_{eq}/M_{eq}}$ is the natural frequency of the device, and R_l is the load resistance.

The governing equations represent the electromechanical behaviour of the simplified lumped mass model in Fig. 2. The lumped-parameter model is represented by the generalised coordinate q and the voltage across the resistor v. The load resistance in Eq. (30) can be replaced by the equivalent resistance R_{eq} obtained from the load resistance R_l and piezoelectric leakage R_p. In general, the equivalent resistance can be approximated by the load resistance because the piezoelectric leakage is much higher. The damping coefficient C_{eq} represents the dissipation of mechanical energy due to the viscous effects of the harvester.

The governing equations can be evaluated in terms of amplitude and phase, assuming a harmonic base excitation of the form $z_b(x_b,t) = z_0(x_b,\overline\omega)\exp(\iota\overline\omega t)$:

$$
(-\overline\omega^2 + 2\iota\overline\omega\zeta\omega + \omega^2)q_0(\overline\omega) - \frac{\alpha}{M_{eq}}v_0(\overline\omega) = \frac{M_{eff}}{M_{eq}}\overline\omega^2 z_0(x,\overline\omega)
\tag{31}
$$

$$
\left(\iota\overline\omega C_p + \frac{1}{R_l}\right)v_0(\overline\omega) + \iota\overline\omega\alpha q_0(\overline\omega) = 0
\tag{32}
$$

where $\overline\omega$ is the frequency of excitation and the imaginary unit number is denoted by the Greek letter ι to avoid confusion with the subscript i used in subsequent derivations. The solution of the previous equations allows us to calculate the amplitudes of displacement and voltage:

$$
q_0(\overline\omega) = \frac{M_{eff}\overline\omega^2 z_0(x,\overline\omega)/M_{eq}}{2\iota\overline\omega\zeta\omega + \omega^2 - \overline\omega^2 + \iota\overline\omega\alpha^2/M_{eq}\left(\iota\overline\omega C_p + 1/R_l\right)}
\tag{33}
$$

$$v_0(\overline{\omega}) = \frac{\iota\overline{\omega}\alpha q_0(\overline{\omega})}{\left(\iota\overline{\omega}C_p + 1/R_l\right)} \tag{34}$$

Eqs. (33) and (34) provide the response of the energy harvester under the base excitation z_0 acting at the frequency $\overline{\omega}$.

The derivation of the former expressions is based on the parameters β, γ and μ that relate the geometry and mechanical properties of the beam section with PZT to the substructure. These parameters facilitate the optimal harvester tuning procedure in the following sections.

2.2. Dynamic behaviour and load resistance

The behaviour of the energy harvester strongly depends on the resistance of the load. Two characteristic frequencies are defined for the short- and open-circuit conditions [40], ω_{sc} and ω_{oc}, respectively. The first frequency corresponds to the natural frequency of the harvester $\omega_{sc} = \omega$, and the other is estimated as $\omega_{oc} = \omega_{sc}\sqrt{1 + d^2 - 2\zeta^2}$ ($d^2 = \alpha^2/(K_{eq}C_p)$), which is higher than the previous. The open-circuit condition corresponds to the antiresonant frequency of the system.

The resonant frequency ω_d depends on the load resistance in addition to the mechanical damping factor. The resonant frequency can be estimated from a complex modal analysis [41] rewriting the governing Eqs. (29) and (30) in free vibration as follows:

$$\begin{bmatrix} 2\zeta\omega & 0 & 1 \\ \alpha & C_p & 0 \\ 1 & 0 & 0 \end{bmatrix}\begin{bmatrix} \dot{q} \\ \dot{v} \\ \ddot{q} \end{bmatrix} + \begin{bmatrix} \omega^2 & -\alpha/M_{eq} & 0 \\ 0 & 1/R_l & 0 \\ 0 & 0 & -1 \end{bmatrix}\begin{bmatrix} q \\ v \\ \dot{q} \end{bmatrix} = \begin{bmatrix} 0 \\ 0 \\ 0 \end{bmatrix} \tag{35}$$

Eq. (35) is reformulated as a first-order matrix equation of the form $\mathbf{A}\dot{\mathbf{w}} + \mathbf{B}\mathbf{w} = 0$, where the non-trivial solution can be expressed as $\mathbf{w} = \Psi e^{st}$. The solution is given by the eigenvalues s and the corresponding eigenvectors Ψ:

$$\Psi = \begin{bmatrix} \phi \\ s\phi \end{bmatrix} \tag{36}$$

The eigenvalue solution provides the modal parameters of the system taking into account the electromechanical coupling effect: (*i*) the natural frequency $\omega_n = |s|$ ($\omega_n \geq \omega$), (*ii*) the resonant frequency $\omega_d = |\text{Im}\{s\}|$, and (*iii*) the damping coefficient $\zeta_d = -\text{Re}\{s\}/|s|$ ($\text{Re}\{s\} < 0$, $\text{Im}\{s\} \neq 0$). The resonant frequency satisfies $\omega_d = \omega_n\sqrt{1 - \zeta_d^2}$. The damping ratio ζ_d accounts for the mechanical and electrical damping of the system and depends on the load resistance as: $\zeta_d = \zeta$ in the short-circuit condition; $\zeta_d < \zeta$ in the open-circuit condition; and the maximum is reached between both cases.

2.3. Output power and optimum load resistance

Once the output voltage is obtained from Eq. (34), the power dissipated by the load resistor $P_0(\overline{\omega}) = v_0(\overline{\omega})^2/R_l$ is:

$$|P_0(\overline{\omega})| = \frac{(M_{eff}/M_{eq})^2\alpha^2 R_l\overline{\omega}^6 z_0^2(x,\overline{\omega})}{(\alpha^2 R_l\overline{\omega}/M_{eq} + C_p R_l\overline{\omega}(-\overline{\omega}^2 + \omega^2) + 2\omega\overline{\omega}\zeta)^2 + (-\overline{\omega} + \omega^2 - 2C_p R_l\overline{\omega}^2\omega\zeta)^2} \tag{37}$$

The optimal load resistance that maximises the output power at the excitation frequency $\overline{\omega}$ is calculated by differentiating and equating Eq. (37) to zero [40]:

$$R_{l,opt}(\overline{\omega}) = \frac{M_{eq}(\overline{\omega}^4 + \omega^4 + 2\overline{\omega}^2\omega^2(-1 + 2\zeta^2))^{1/2}}{(-\overline{\omega}^2(\alpha^2 + C_p M_{eq}(-\overline{\omega}^2 + \omega^2))^2 - 4C_p^2 M_{eq}^2\overline{\omega}^4\omega^2\zeta^2)^{1/2}} \tag{38}$$

The maximum output power is obtained at the short-circuit frequency for the load resistance $R_{l,opt}(\omega_{sc})$. The resonant frequency ω_d for the optimum load resistance is given by the solution of Eq. (35). The resonant frequency deviates slightly from the natural frequency ω and can be approximated by $\omega_d = \omega$.

2.4. Optimal tuning procedure

The performance of the device is limited to a narrow band around the resonant frequency, and then the power is drastically reduced if the excitation frequency deviates from resonance. The procedure for adjusting the resonant frequency of the harvester to the fundamental mode shape of the bridge is described in detail below.

The methodology adopted consists of: (*i*) the harvester tuning frequency is set to the fundamental frequency of the bridge ω_{b1}, therefore $\omega_d = \omega_{b1}$; and (*ii*) the damping coefficient $C_{eq} = 2\zeta\sqrt{K_{eq}M_{eq}}$ is the same regardless of the bridge to which the harvester is tuned, allowing a comparable analysis of the collected energy [18]. The last condition is satisfied by defining the design parameter $r = K_{eq}M_{eq}$. All the above and the parameter γ allow determining the thickness and length of the substructure, h_s and L_s, and the tip mass M_t to adjust the harvester to the fundamental frequency of the bridge.

The tuning procedure optimise the power dissipated by the load resistance under resonant conditions setting $\overline{\omega} = \omega_{b1}$ in Eq. (37). The maximum amplitude of the harmonic base excitation is limited to $\ddot{z}_0(\overline{\omega}) = 3.5\,\text{m/s}^2$, which corresponds to the maximum acceleration level allowed on ballast railway bridges [37]. The harvester must withstand the stress in the substructure under this load, ensuring $\sigma_x(x) \leq \sigma_y$, where σ_y is the yield stress or the tensile strength. Several analyses have shown that the cross section in

Table 1
Geometry and material properties of the energy harvester.

Property	Symbol	Value
Piezoelectric density	ρ_p [kg/m^3]	7800
Substructure density	ρ_s [kg/m^3]	9000
Piezoelectric Young's modulus	c_{11}^E [GPa]	66.23
Substructure Young's modulus	E_s [GPa]	105
Piezoelectric constant	e_{31} [N/Vm]	−12.6
Vacuum permittivity	ϵ_0 [F/m]	8.854×10^{-12}
Absolute permittivity	ϵ_{33}^S [F/m]	$1530\epsilon_0$
Plate length	L_p [mm]	50.8
Plate width	b_p [mm]	31.8
Beam length	L_s [mm]	$L_p = L_s$
Beam width	b_s [mm]	$b_s = b_p$
Piezoelectric thickness	h_p [mm]	0.26
Substructure thickness	h_s [mm]	0.14
Damping ratio	ζ [%]	2.7
Tip mass	M_t [g]	12

which the maximum stress is reached is found at $x = L_p$ ($\beta \leq 1$), which is located in the section of the substructure without PZT closest to the fixed end.

The printing volume of a 3D printer limits the maximum length of the substructure. The maximum length of the substructure is constrained to $L_{s,max} = 0.3$ m, which would be valid for most commercial 3D printers.

Then, the optimisation problem is defined as follows:

$$\underset{r,\gamma}{\text{maximise}} \quad |P_0(\omega_{b1})|$$

$$\text{subject to} \quad \sigma_x(L_p) \leq \sigma_y, \quad L_s \leq L_{s,max}$$

The optimal solution is obtained using a genetic algorithm that starts to tune random individuals given by r and γ to the fundamental frequency of the bridge. Here, the tuning frequency is given by the dynamic behaviour of the bridge. The design parameters h_s, L_s, and M_t are calculated from the tuning frequency and the parameters r and γ. Then, the resonant frequency of the system and the load resistance are obtained from Eqs. (35) and (38), respectively. Finally, the output power is evaluated if the constraints of the problem are satisfied for the design. This process is repeated in subsequent generations to find the optimal design of the harvester.

3. Verification of the proposed model

The proposed lumped parameter model was verified by considering a bimorph beam consisting of two PZT-5 A patches glued to a brass substructure. The tuning frequency of the system was 45.7 Hz. Table 1 summarises the geometry and material properties of the energy harvester.

The properties of the piezoelectric material are obtained from the data sheet provided by the manufacturer of PZT-5 A [42] and the expressions for the elastic modulus c_{11}^E, the electromechanical constant e_{31}, and the permittivity under constant strain ϵ_{33}^S according to the assumption of plane stress [39].

This system was previously analysed by Ertuk and Inman [39] using a coupled distributed model. The governing equations proposed in [39] are based on the Euler–Bernoulli beam assumptions and solved by modal superposition. The mode shapes corresponded to a uniform cantilever beam considering $L_p = L_s$ ($\beta = 1$). Next, the governing equations derived in the previous section are verified against the solution in [39] and compared with the results of a two-dimensional (2D) finite element (FE) model.

The FE model was implemented in ANSYS [43] using: (*i*) PLANE223 elements for piezoelectric patches; (*ii*) PLANE183 to represent the substructure; (*iii*) a CIRCU94 element for the load resistance, and (*iv*) the MASS21 for the mass of the tip. The PLANE223 is an eight-node coupled field solid element with three degrees of freedom (in-plane displacements and voltage), PLANE183 is an eight-node solid element, CIRCU94 is used for piezoelectric circuits, and MASS21 is a structural mass element. In the analysis, the plain stress formulation was used instead of the three-dimensional one [44,45] to reduce the computational cost.

First, three different configurations were studied: (*i*) short circuit condition ($R_l = 1$ kΩ), (*ii*) optimal resistance condition ($R_l = 33$ kΩ), and (*iii*) open circuit condition ($R_l = 470$ kΩ). Fig. 3 shows the frequency response functions (FRF) of the acceleration of the tip and the output voltage. The response was maximum at the resonant frequency. Maximum acceleration occurred in the short-circuit condition, whereas maximum voltage was found in the open-circuit condition. The resonant and antiresonant frequencies were also represented in the plots. The results agree with the FE analysis and the solution proposed in [39].

The largest differences between the computed results occur in open-circuit condition for both the acceleration and the voltage. The maximum acceleration computed with the proposed model is 156.50 m/s^2/g, while the reference solution [39] is 157.34 m/s^2/g and the numerical result equals 155.46 m/s^2/g. On the other hand, the maximum voltage in open-circuit condition is 94.34 V/g, that agrees the reference solution 93.97 V/g [39] and the numerical result 89.07 V/g. In other situations, the discrepancies between the models are much lower.

The performance of the original harvester was then compared with the design resulting from the tuning procedure described in Section 2.4. The lower and upper limits of the optimisation variables were $r \in [0.1, 50]$ and $\gamma \in [1.1, 50]$. The initial population
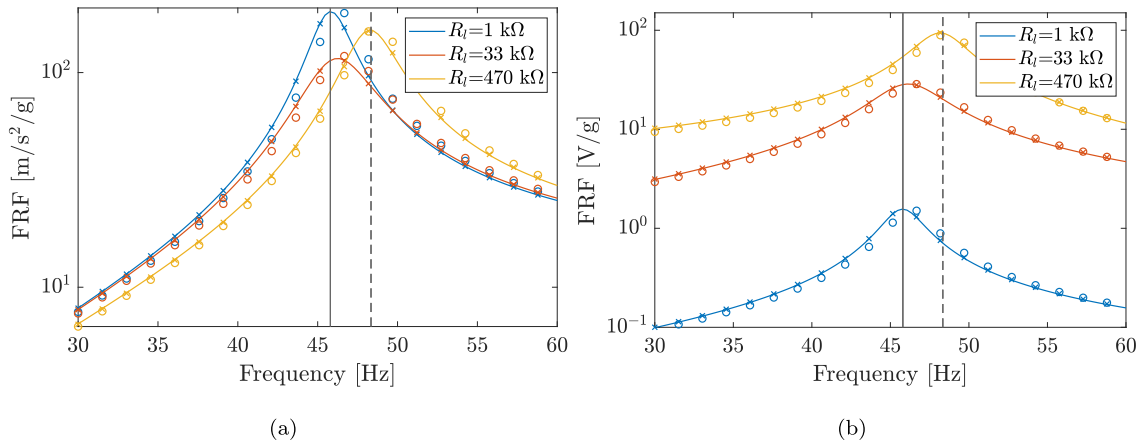
Fig. 3. Frequency response function of (a) the tip acceleration and (b) voltage for three different values of the load resistance. Comparison of the proposed solution (crosses), reference solution [39] (solid line) and the finite element results (circles). Resonant and antiresonant frequencies are represented by vertical grey solid and dashed lines, respectively.
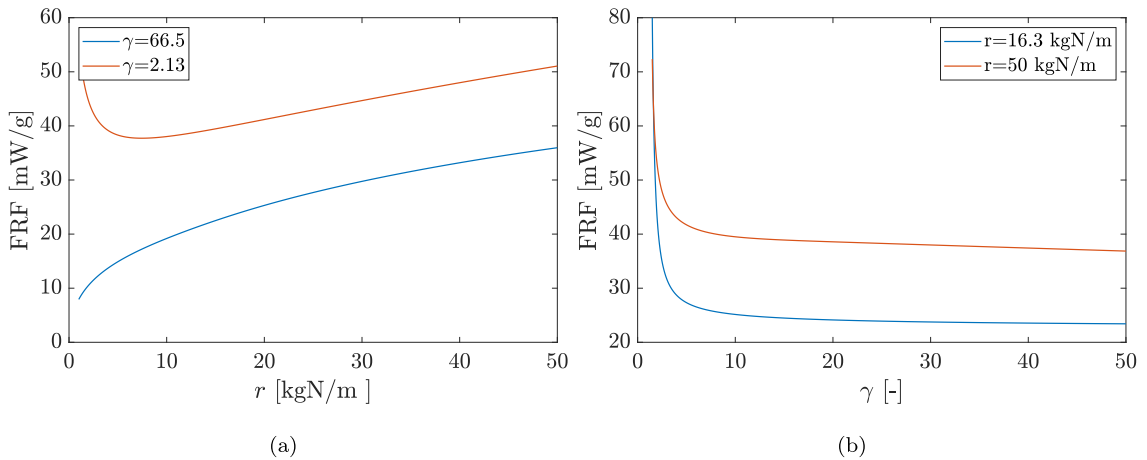

Fig. 4. Output power at the resonant frequency dissipated by the load resistance $R_l = 33\,\mathrm{k\Omega}$ for (a) fixed γ values and (b) fixed r values.

was 50, the crossover fraction was 0.8, and the elite children were 3 in each generation. The optimal solution was obtained after 4 generations given $r = 50\,\mathrm{kgN/m}$ and $\gamma = 2.13$. The optimal reached the upper limit of the parameter r due to the output power increases with r. The upper limit will be taken if the structural integrity criterion is achieved. However, an increase in r would lead to a non-realistic design with high mass. The optimal load resistance given by Eq. (38) has changed from the original configuration, obtaining $R_l = 54.11\,\mathrm{k\Omega}$.

The geometry of the substructure resulting from the optimal tuning design is defined by $h_s = 1.3\,\mathrm{mm}$, $L_s = 114.7\,\mathrm{mm}$ and $M_t = 15.7\,\mathrm{g}$. In this case, the value of the geometry parameter $\beta = L_p/L_s = 0.44$ makes the solution proposed by Ertuk and Inman [39] not valid, which means that the PZT fully covers the substructure.

The harvester performance can be better understood by analysing the influence of the optimisation variables on the output power. The initial configuration was characterised by $\beta = 1$, $r = 16.3\,\mathrm{kgN/m}$ and $\gamma = 66.5$ according to the properties of Table 1. Fig. 4 shows the power at the resonant frequency dissipated by the optimal load resistance $R_l = 33\,\mathrm{k\Omega}$ for (i) $0.1 \leq r \leq 50$ and $\gamma = [2.13, 66.5]$ (Fig. 4.(a)) and (ii) $r = [16.3, 50]\,\mathrm{kgN/m}$ and $1.1 \leq \gamma \leq 50$ (Fig. 4.(b)). The output power increases as r is higher and γ lower. The results for $r \leq 10$ and $\gamma = 2.13$ (Fig. 4.(a)) are not realistic since in the range of the asymptotic behaviour the mass at the tip becomes negative.

Fig. 5 compares the dimensional shape function $\psi(x)$ and the slope for the optimal design with those computed from the first mode shape obtained using the FE analysis. The discontinuity in the slope at the coordinate $x = L_p = 0.05\,\mathrm{m}$ denotes the change in bending stiffness from the beam section with PZT to the substructure. The agreement between both sets is good.

Fig. 6 shows the frequency response functions for the optimal design calculated from the proposed analytical solution and the FE model. The results show that the maximum acceleration of the tip and the output voltage were slightly higher than in the initial configuration. In this case, the maximum acceleration in open-circuit condition is $196.5\,\mathrm{m/s^2/g}$, whereas the numerical result is
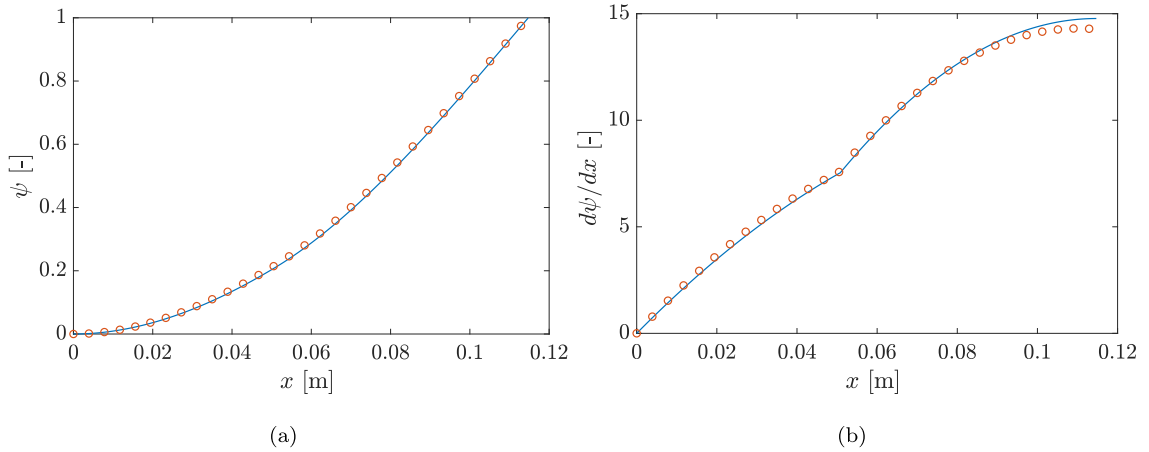
Fig. 5. Comparison of proposed results (solid line) and FE analysis (circles) for (a) the dimensional shape function $\psi(x)$ and (b) the related slope.
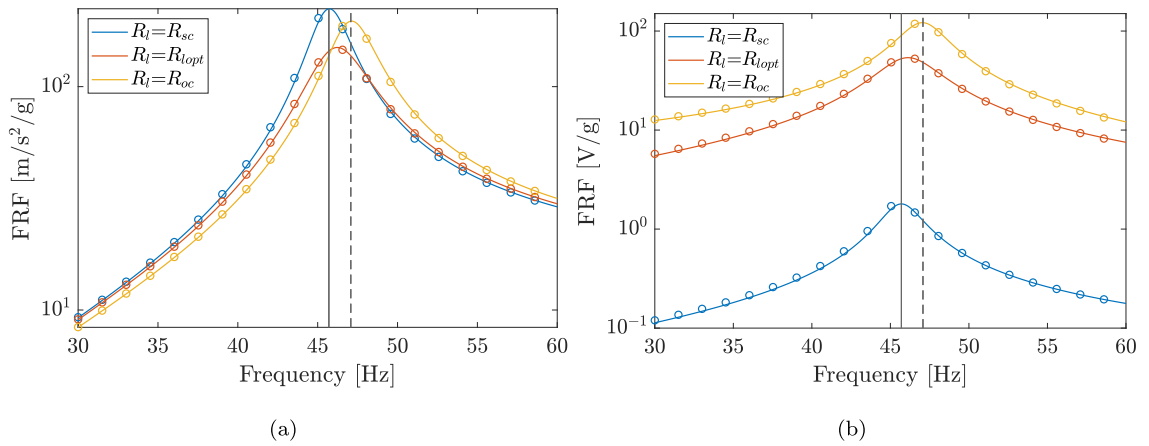

Fig. 6. Frequency response function for the optimal design of (a) the tip acceleration and (b) voltage, for three different values of load resistance. Comparison of the proposed solution (solid line) and the finite element results (circles). Resonant and antiresonant frequencies are represented by vertical grey solid and dashed lines, respectively.

186.9 m/s²/g. The maximum voltage is 121.55 V/g and the numerical result 118.36 V/g. Also, the output power was higher in the new configuration, as can be seen in Fig. 7. The major differences of both solutions are provided for the optimal load resistance, where the power obtained for the optimal design is 53.58 mW/g and the power obtained from the original design is 2.534 mW/g [39]. The solution of the complex modal analysis showed that the damping increased from mechanical ratio $\zeta = 2.7\%$ to $\zeta_d = 4.1\%$ due to the load resistance, and the resonant frequency became 46.14 Hz.

4. Case study

In this section, energy harvesting on a High-Speed railway bridge is analysed using experimental records. The content of this section covers: (*i*) identification of the tuning frequency; (*ii*) optimal design and manufacturing of the harvester; (*iii*) experimental estimation and validation of the FRF for tip acceleration and voltage; and (*iv*) assessment of the energy harvesting from railway traffic.

4.1. Tuning frequency in forced vibration

In May 2019, the authors performed an experimental campaign on several railway bridges, including the identification of modal parameters and the recording of vibration levels under operating conditions [46]. Jabalón HSL Bridge (Fig. 8) was selected from the experimental campaign. This bridge is composed of three identical simple supported bays of equal span lengths $L_b = 24$ m (Fig. 8). Each deck consists of a concrete slab with dimensions 11.6 m × 0.3 m (width × thickness). The structure crosses Jabalón River with a skew angle of 134°. Fig. 8 shows the sensor layout in the first span.
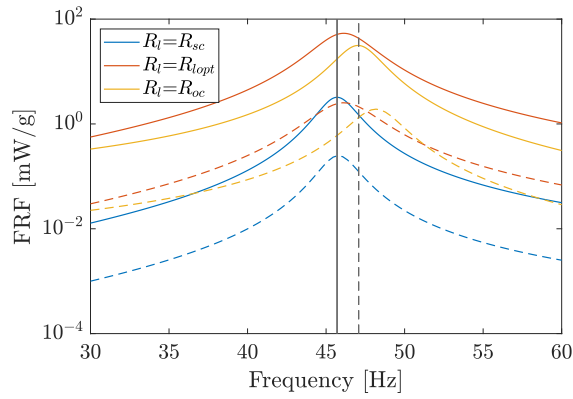
Fig. 7. Frequency response function of the output power for three different values of the load resistance. Comparison of the optimal design (solid line) and the initial configuration (dashed line). Resonant and antiresonant frequencies are represented by vertical grey solid and dashed lines, respectively.

Fig. 8. HSL bridge over Jabalón River (38°53′51.3″N 3°57′53.0″W): (a) general view, (b) transducer setup, and (c) scheme of the experimental setup.

The modal parameters of the bridge were identified from the ambient vibration data using the Stochastic Subspace Identification technique [47]. The fundamental mode corresponds to the first longitudinal bending mode with natural frequency $f_{b1} = 6.3$ Hz and modal damping $\zeta_{b1} = 3.2\%$. Although this estimated natural frequency can be chosen as the tuning frequency, the analysis of the vibrations produced by the railway traffic showed that the response was dominated by a slightly lower frequency. Fig. 9 shows the bridge response induced by a Renfe S102 train that circulates at $V = 274$ km/h. The frequency content has a predominant peak at 5.68 Hz, which is lower than the natural frequency of the bridge $f_{b1} = 6.3$ Hz. The fundamental frequency of the bridge is indicated with a vertical line. The difference between the first natural frequency and the identified peak of forced vibrations was due to the effect of the train mass on the response of the bridge. Romero et al. [18] showed that harvested energy in railway bridges by a detuned device is drastically reduced for a frequency deviation higher than 5%. Therefore, the tuning frequency must be slightly lower than the first natural frequency to avoid a reduction in harvester performance. The value 5.68 Hz is used in the following as the tuning frequency.
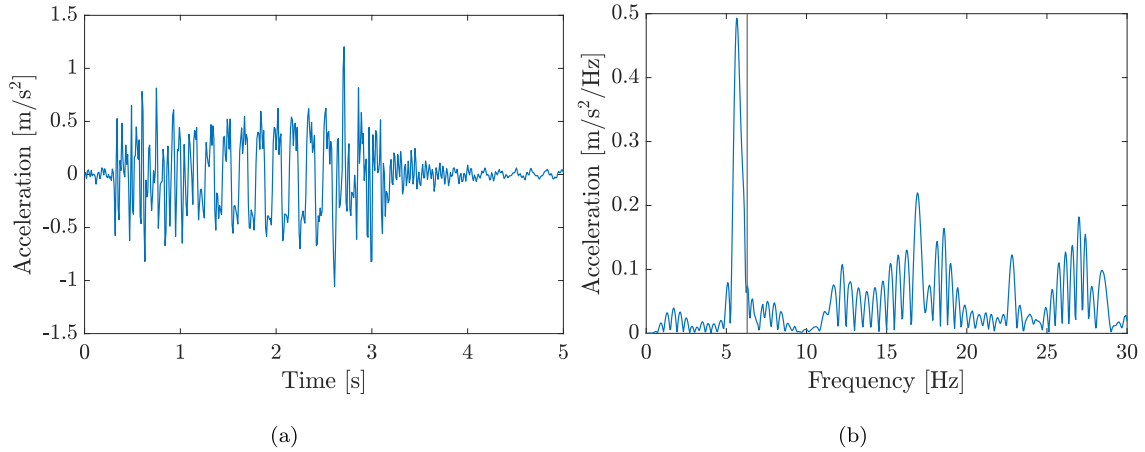
Fig. 9. (a) Time history and (b) frequency content of the bridge acceleration at point $A7$ induced by Renfe S102 train circulating on track 2 at $V = 274\,\text{km/h}$ (passage #11). The vertical line represents the first natural frequency of the bridge.

Furthermore, the maximum instantaneous acceleration was less than $1.5\,\text{m/s}^2$, while the peak acceleration at $5.68\,\text{Hz}$ was less than $0.5\,\text{m/s}^2/\text{Hz}$. These were both lower than the maximum acceleration value $3.5\,\text{m/s}^2$ considered in the tuning procedure in Section 2.4. A decrease in the maximum value of the acceleration in the optimal tuning design produces slender structures as the stress is reduced, with a subsequent increase in the harvested energy. Therefore, the maximum value that the harvester must withstand will be limited to $1.5\,\text{m/s}^2$ in the tuning procedure.

The characteristic tuning frequency and the maximum allowable acceleration are representative of all train passages recorded in the experimental campaign at sensor locations [46].

4.2. Harvester design and manufacturing

The selected PZT patch is the commercial DuraAct patch transducer P-876.A12 [48], composed of a piezoelectric layer covered by copper electrodes. The patch is embedded in a structure mechanically pre-stressed by a polymer surface, making it flexible. Patch dimensions are $L_p = 50\,\text{mm}$, $b_p = 30\,\text{mm}$ and $h_p = 0.2\,\text{mm}$. The properties of the PZT material are $c_{11}^E = 123\,\text{GPa}$, $e_{31} = -7.15\,\text{N/Vm}$, $\epsilon_{33}^S = 857\epsilon_0$ and $\rho_p = 7800\,\text{kg/m}^3$.

P.876-A12 patches work in the 31 mode and are polarised along the thickness. Furthermore, for the purpose of this research, the patches are connected in series. In the bimorph configuration, the series connection requires the patches to be polarised in opposite directions. Then, they are glued with the negative electrode towards the substructure and the series connection is done by connecting positive and negative electrodes. The load resistance is connected to the positive electrodes of the series connection.

An additive manufacturing material has been selected for the substructure. Among the variety of 3D printing materials, the feasibility of polylactic acid (PLA), acrylonitrile butadiene styrene (ABS), thermoplastic polyurethane (TPU) and high temperature polyamide carbon fibre reinforced (PAHT CF15) materials were analysed. PLA and ABS are the most common 3D printing materials, TPU is a flexible polymer, and PAHT CF15 is often used to replace metals in some applications due to its high strength. Therefore, the selected materials facilitate the study of the performance of the harvester for a wide range of substructure stiffnesses. Table 2 shows the mechanical properties of the ABS, PAHT-CF15 and PET-CF15 printing filaments provided by BASF [49], and those given by Mitsubishi Chemical Performance Polymers (MCPP) [50] for PLA and TPU.

The optimisation problem was solved for the input parameters defined in the intervals $r \in [0.1, 20]\,\text{kgN/m}$ and $\gamma \in [1.1, 200]$. The damping ratio was set to $\zeta = 1\%$ in all cases. The results of the optimal design are summarised in Table 2. Fig. 10 shows the frequency response functions of the output power for optimal designs. The PAHT CF15 design exhibits the best performance with output power in resonant condition $|P_0(\omega_{b1})| = 1909.7\,\text{mW/g}$, while the TPU yields the worst performance. PLA and ABS designs were very similar. The analysis also included a brass design as a reference. In this case, the output power was higher than in the 3D printing designs because of the higher stiffness of the brass substructure.

The previous results show that PAHT CF15 is the most suitable printing material for the substructure. However, carbon fibre-reinforced materials need to have appropriate nozzles made of a special alloy to avoid fast hotend deterioration or damage. Therefore, PLA was selected as the substructure material instead of PAHT CF15 because it is one of the most widely used materials in 3D printing due to its low cost and ease of printing. Furthermore, PLA is a thermoplastic material derived from crops such as corn, cassava, and sugarcane, making it a sustainable and biodegradable material with a low environmental impact.

Before the design and manufacturing of the harvester, the mechanical properties of PLA were estimated to assess the influence of the printing configuration. The mechanical properties of five PLA printed specimens using a hotend with a nozzle of $0.6\,\text{mm}$ were estimated according to the ASTM D638-14 standard [51] (Fig. 11). The infill was 100%, the printing temperature was 200 °C with a build plate temperature of 45 °C, and the print and travel speeds were $45\,\text{mm/s}$ and $200\,\text{mm/s}$, respectively. Fig. 11(b) shows

Table 2
Mechanical properties and optimal design parameters of printing materials (brass design is include as reference).

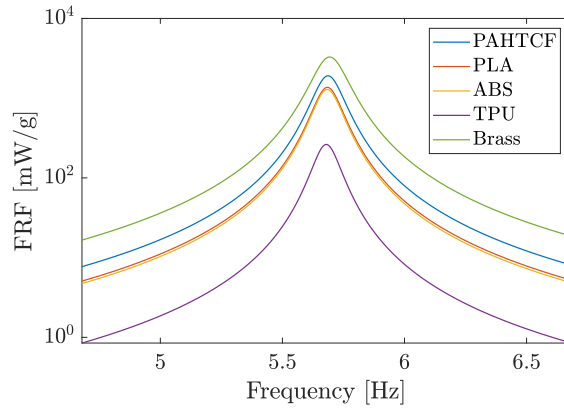| Property	Units	PAHT-CF15	PLA	ABS	TPU	Brass
E_s	GPa	5.052	3.12	2.6	0.15	105
ρ_s	kg/m^3	1232	1240	1040	1160	9000
σ_y	MPa	125.4	70	48.6	50	255
h_s	mm	0.8	1.6	1.7	5.3	0.9
L_s	mm	95.4	131.3	132.7	151.7	178.6
M_t	g	125	124	124	121	117
R_l	kΩ	944	967	969	984	837
α	N/V $\times 10^4$	1.64	1.32	1.27	0.53	2.37
r	kgN/m	20	20	20	20	20
γ	–	62.82	40.42	42.67	200	3.51
$|P_0(\omega_{b1})|$	mW/g	1909.7	1368.6	1287.0	263.5	3288.7

Fig. 10. Frequency response function of the power for five different substructure materials at each optimal design.
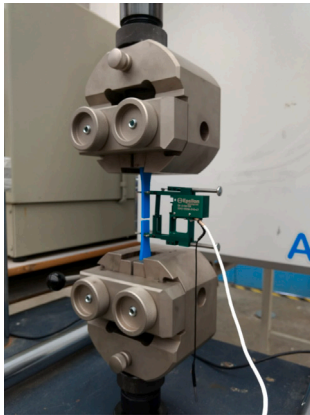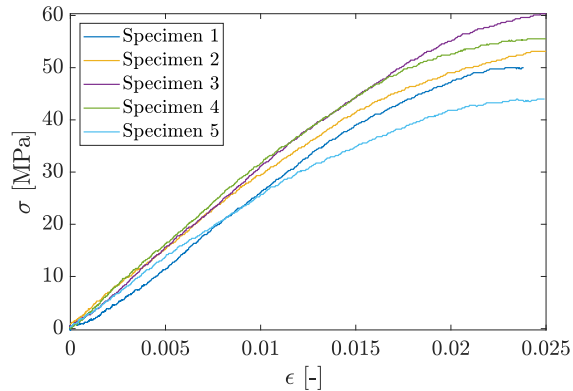
(a)　　　　　　　(b)

Fig. 11. (a) Experimental setup and (b) results of the tensile test.

the results of the tensile tests. The material properties were: mean Young's modulus $E_s = 2.95$ GPa with a standard deviation of $s_E = 0.28$ GPa; and tensile strength $\sigma_y = 53$ MPa with a standard deviation of $s_\sigma = 6.35$ MPa. The estimated properties were lower than the nominal values in Table 2 and were used in the following. A safety factor $\gamma_G = 1.33$ was used to assess structural integrity in the optimisation procedure to account for the standard deviation of tensile strength.

The optimal PLA design was then defined by $L_s = 158.6$ mm, $h_s = 2.1$ mm, and $M_t = 123$ g. The load resistance was $R_l = 970$ kΩ, providing an output power $|P_0(\omega_{b1})| = 1285$ mW/g. The solution of the optimisation problem was $r = 20$ kgN/m and $\gamma = 28.9$. The energy performance is related to the substructure and the deformation of the PZT, and then the optimal design was obtained for a substructure that reached the maximum allowable stress $\sigma_y/\gamma_G = 39.8$ MPa.
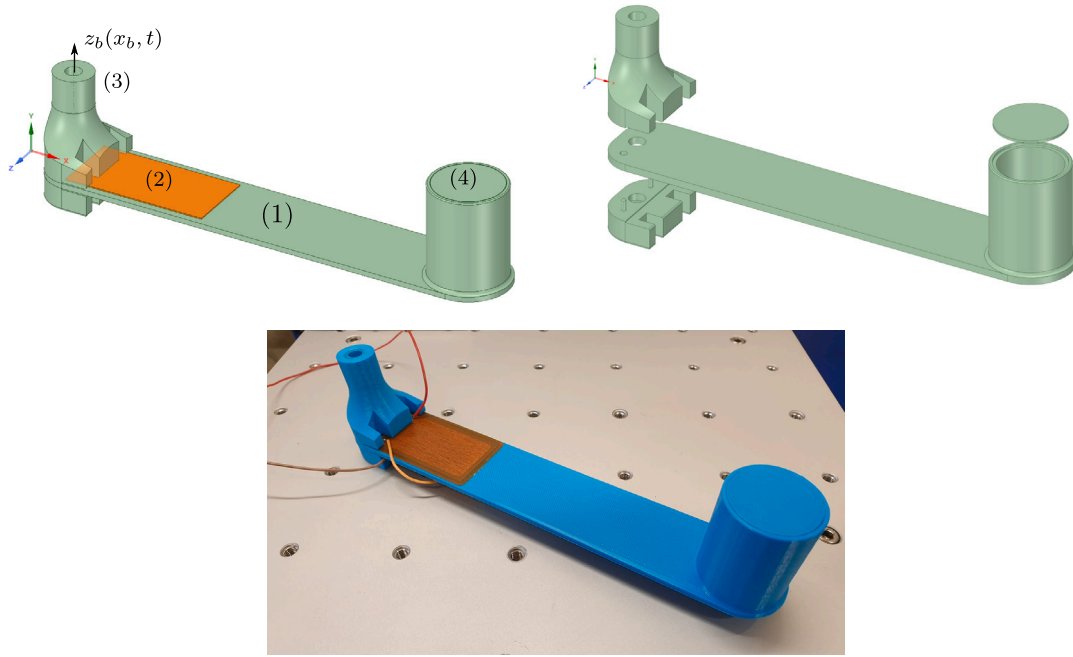
Fig. 12. CAD model, exploded view and printed prototype: (1) substructure, (2) PZT patches, (3) clamp and (4) mass storage.

The design was implemented in `ANSYS SpaceClaim` and was numerically verified in `ANSYS Mechanical` (see Fig. 12). The geometry consisted of the substructure, the piezoelectric patches, a clamp to attach the harvester to the bridge, and a hollow cylinder for the tip mass. The connection point to the bridge is denoted by the displacement $z_b(x_b, t)$. Fig. 12 also shows the printed prototype with the piezoelectric patches glued to the substructure.

4.3. Experimental validation

The printed prototype was experimentally validated by comparing the analytic frequency response functions for the tip acceleration and output voltage given by Eqs. (33) and (34). The experimental test consisted of measuring the response of the device due to the base excitation induced by an APS 400 ELECTRO-SEIS electrodynamic shaker (see Fig. 13). A Brüel & Kjaer LAN-XI data acquisition system was used to perform the Analog/Digital conversion at a sampling frequency $f_s = 2048$ Hz. The tip velocity was measured by an Ometron VH-1000-D laser vibrometer with nominal sensitivity 8 V/m/s, and the output voltage was recorded directly with the acquisition system. Furthermore, the base acceleration was measured with a PCB 352C33 accelerometer with nominal sensitivity 100 mV/g. The device was subjected to a burst random acceleration in a 50 Hz bandwidth during 128 s. The burst percentage was set to 50% of the total test time. Fig. 14 shows the time records.

The frequency response functions were estimated by averaging the results of five tests. A preliminary analysis showed that the tip mass should be corrected by adding 21 g to obtain the tuning frequency. Fig. 15 shows the experimental FRF and the analytical solution for tip acceleration and voltage. The discrepancies between both sets were investigated by fitting the analytical solution to the experimental response. The Levenberg–Marquardt nonlinear least squares algorithm [36] is used to fit the frequency response function for acceleration and tip voltage to the experimental results, and the damping coefficient ζ and the coupling factor α in Eqs. (33) and (34) are then obtained. Fig. 15 shows the acceleration and voltage resulting from the fitting process. The update parameters were the damping ratio and the electromechanical coupling coefficient (see Eqs. (33) and (34)). The experimentally estimated values were $\zeta_{Exp} = 0.69\%$ and $\alpha_{Exp} = 1.44 \times 10^{-4}$ N/V. The damping ratio was lower than the value $\zeta = 1\%$ used in the design, and the coupling coefficient was slightly higher than the analytical estimation $\alpha = 1.27 \times 10^{-4}$ N/V given by Eq. (A.6), probably due to uncertainties in the pre-stress and adhesive properties of the patch.

The damping ratio plays an important role in the harvester design because the maximum acceleration level in resonant conditions is determined by this value, and therefore the maximum stress in the substructure. A reduction in the damping ratio with respect to the initial design will produce an increase in the substructure stress. Therefore, the thickness h_s must be increased to withstand the stress in the substructure, and consequently the length L_s must be increased to ensure the tuning of the device. A new harvester was designed using the identified experimental damping value. The new design is the result of a retrofit strategy. The solution was $r' = 20$ and $\gamma' = 19.7$, corresponding to $L'_s = 203.9$ mm, thickness $h'_s = 3$ mm, mass $M'_t = 121$ g and load resistance $R'_l = 959$ kΩ. The maximum stress $\sigma_x(L_p)$ reached the maximum allowable value as in the initial design. The coupling coefficient $\alpha' = 1.22 \times 10^{-4}$ N/V was similar to the initial design, but the output power under resonant conditions $|P'_0(\omega_{b1})| = 2377$ mW/g was much higher than the initial value $|P_0(\omega_{b1})| = 1285$ mW/g, since a decrease in damping produces an increase in power, as can be deduced from Eq. (37).

Fig. 13. Experimental setup.
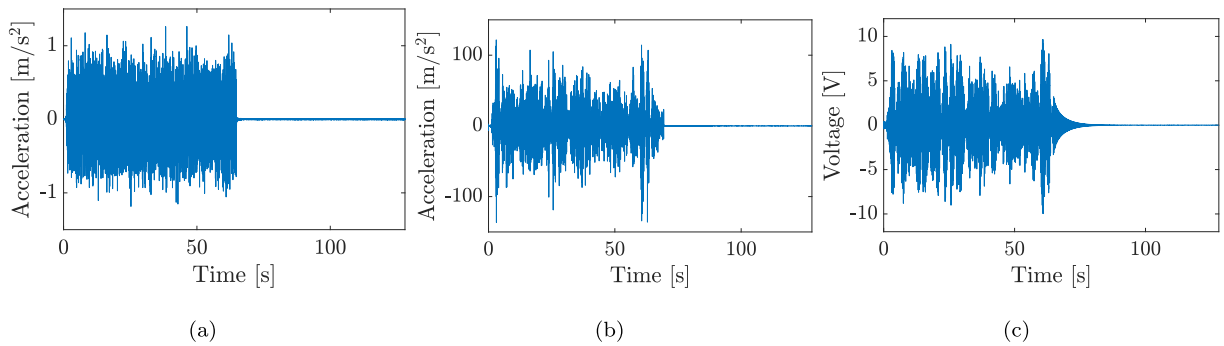

(a)

(b)

(c)

Fig. 14. Test time records of (a) acceleration of the base, (b) acceleration of the tip and (c) output voltage.

The device was experimentally validated following the procedure described above. Fig. 16 shows the comparison of the experimental and analytical frequency response functions of the retrofitted design. Again, the tip mass was adjusted by adding $10\,\mathrm{g}$ to obtain the tuning frequency, resulting in strong agreement. The new estimation of the damping ratio and the coupling coefficient, $\zeta'_{Exp} = 0.69\%$ and $\alpha'_{Exp} = 1.29 \times 10^{-4}\,\mathrm{N/V}$, is consistent with the analytical model ($\alpha' = 1.22 \times 10^{-4}\,\mathrm{N/V}$). A new retrofit of the design using the estimated damping ζ'_{Exp} did not produce significant changes in the substructure geometry or power.

4.4. Energy harvesting from railway traffic

Twenty passenger train circulations were recorded on 8 May 2019 between 11:52 and 15:24 hours over Jabalón HSL bridge. All trains were RENFE High-Speed services, and the identified travel speeds V, the average axle loads of the passenger coaches P_k and the train movements are summarised in Table 3. More details can be found in Ref. [46].

The energy harvested for train passages was estimated from the experimental FRF identified in the previous section and the bridge response [18]. Table 3 provides the estimated energy harvested for each train passage and sensor locations. The energy levels varied in a wide range depending on the sensor location and the train passage. The overall analysis shows that the maximum energy was obtained at the central point of the midspan ($109.32\,\mathrm{mJ}$ at point $A6$), while the minimum levels occurred near the
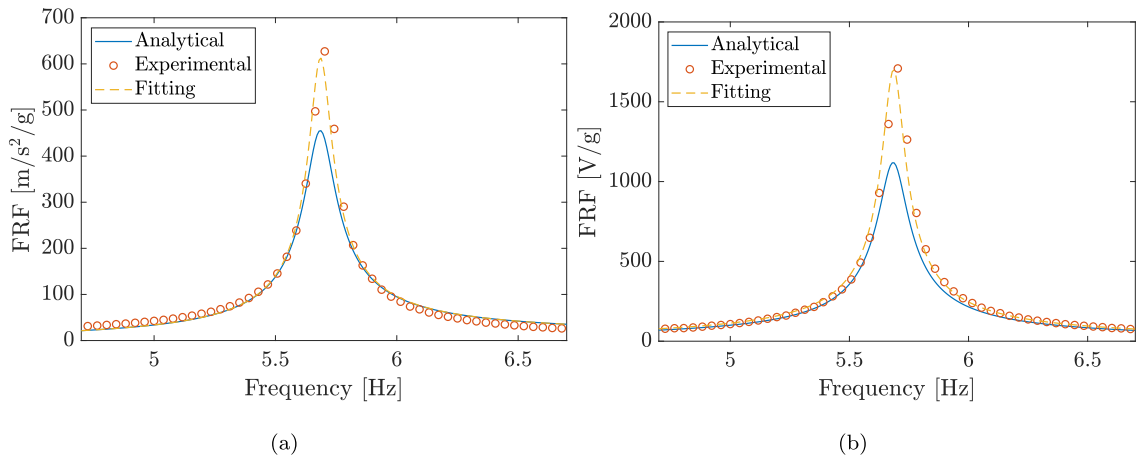
Fig. 15. Analytical and experimental frequency response function of (a) tip acceleration and (b) voltage.
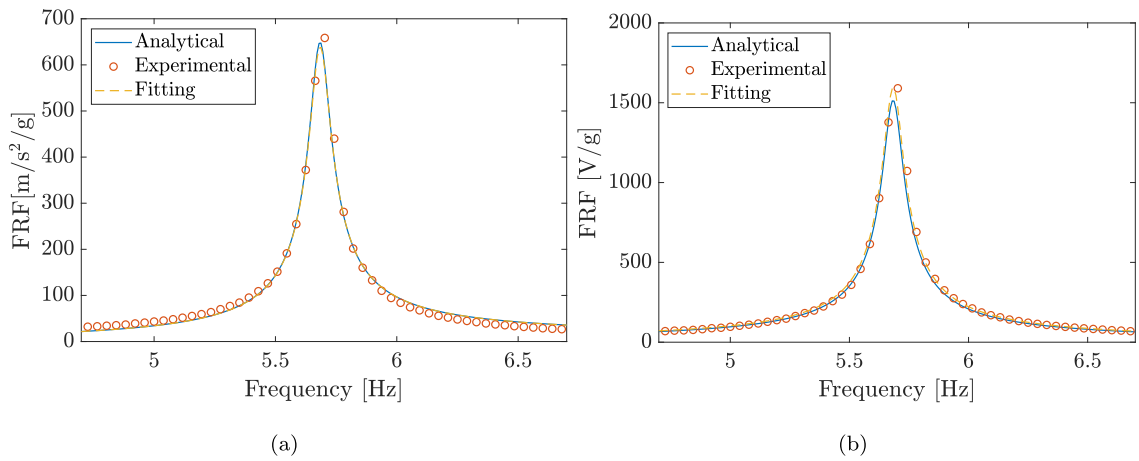

Fig. 16. Analytical and experimental frequency response function of (a) tip acceleration and (b) voltage of the retrofitted design.

supports (0.93–8.34 mJ at points A12–15). This result is consistent with the fundamental mode shape of the bridge [46], in which the maximum amplitude was found at the midspan. The maximum energy is obtained from duplex configurations of the trains. There is not a clear influence of the circulating track or the train speed on the energy levels.

Two characteristic train movements were analysed to study differences in the harvested energy. Passage #3 was one of the lowest energy movements, corresponding to a Renfe S104 train travelling on track 2 at $V = 251$ km/h, and the passage #11 corresponding to a Renfe S102 train travelling on track 2 at $V = 274$ km/h was one of the highest energy movements for simple train configurations. Figs. 17 and 18 show the bridge and harvester accelerations, voltage, and instantaneous power induced by these trains at point A7. The data presented in these figures are computed from the experimental frequency response functions obtained in the laboratory test and the acceleration measurements on the bridge during train passages. The DIN 45672 standard [52] was used to fix the time period T as the part of the signal where the root mean square value exceeds a noise level defined by a heuristic algorithm. The average power was computed as $P_{av} = E/T$ in the time period T. The frequency content of the harvester acceleration shows a sharp peak at the tuning frequency in both cases. However, the frequency content of the harvester acceleration for movement #3 only shows minimal amplification because the fundamental mode shape of the bridge was not excited during the train passage. In the second case, the frequency content of the bridge acceleration was found in the vicinity of the fundamental frequency to which the harvester is tuned. The system response was highly amplified and exhibited resonant behaviour, as was also observed in the voltage and power time histories. The maximum acceleration level of the harvester reached 12.89 m^2/s^2, the maximum voltage 31.18 V, and the average power 0.38 mW. This behaviour can be considered as the optimal performance of the harvester. Consistent results were obtained for the remaining train passages.

The results of this section show that the maximum energy that could be obtained from the train passages is 109.32 mJ at point A6. Using multiple harvesters, the output energy can be increased according to the requirements of a monitoring system. For example, the energy obtained at points A1–A11 could be 471.67 mJ.

Table 3
Energy harvesting [mJ] in train passages recorded at Jabalón HSL Bridge.

| Passage	Train	Track	V [km/h]	P_k [kN]	A1	A2	A3	A4	A5	A6	A7	A8	A9	A10	A11	A12	A13	A14	A15
1	S102	1	290	165	2.53	4.69	2.34	9.00	3.78	12.07	2.41	2.73	0.82	1.45	0.85	0.14	0.32	0.03	0.48
2	S102	2	266	165	0.03	0.05	0.02	0.08	0.06	0.28	0.25	0.24	0.15	0.50	0.08	0.00	0.05	0.00	0.00
3	S104	2	251	153	0.00	0.01	0.00	0.01	0.01	0.03	0.03	0.03	0.01	0.05	0.02	0.00	0.00	0.00	0.00
4	S112-Duplex	1	267	172	6.57	12.89	6.40	4.26	10.38	24.99	6.56	7.46	2.21	3.92	2.31	0.63	0.50	0.09	0.68
5	S102	1	240	165	0.04	0.08	0.04	4.23	1.07	1.34	0.04	0.04	0.01	0.02	0.01	0.04	0.06	0.00	0.56
6	S102-Duplex	2	263	165	0.47	1.16	0.51	2.67	1.96	10.19	8.42	14.05	6.33	5.92	5.61	0.04	1.89	0.26	0.10
7	S100	1	290	156	0.13	0.25	0.13	2.29	0.19	0.37	0.13	0.14	0.05	0.08	0.05	0.03	0.06	0.00	0.18
8	S112	1	269	172	2.36	4.68	2.33	3.08	3.82	9.73	2.42	2.75	0.83	1.46	0.86	0.11	0.10	0.03	0.23
9	S102-Duplex	2	265	165	0.55	1.35	0.60	3.08	2.27	8.72	11.50	11.31	7.21	9.15	10.48	0.04	3.63	0.24	0.11
10	S130	1	236	165	0.05	0.09	0.04	1.25	0.19	0.59	0.04	0.04	0.01	0.02	0.01	0.03	0.03	0.00	0.04
11	S102	2	274	165	0.26	0.63	0.28	1.39	1.03	7.09	4.83	5.01	3.14	4.47	2.24	0.02	0.34	0.07	0.05
12	S102-Duplex	1	267	165	6.36	12.48	6.24	3.04	9.42	23.39	6.28	7.15	2.12	3.77	2.22	1.75	0.19	0.09	0.88
13	S130	2	237	165	0.01	0.03	0.01	0.05	0.04	0.20	0.17	0.39	0.10	1.96	0.15	0.00	0.11	0.00	0.00
14	S104	1	249	153	0.01	0.02	0.01	0.22	0.02	0.56	0.01	0.01	0.00	0.00	0.00	0.00	0.05	0.00	0.00
15	S100	2	262	156	0.04	0.10	0.05	0.19	0.14	0.89	0.53	3.09	0.81	6.88	1.33	0.00	0.01	0.01	0.01
16	S130	1	236	165	0.03	0.06	0.03	1.92	0.06	0.70	0.03	0.03	0.01	0.02	0.01	0.03	0.73	0.00	0.01
17	S100	1	290	156	0.11	0.23	0.11	2.50	0.69	0.45	0.12	0.13	0.04	0.07	0.04	0.11	0.07	0.00	0.17
18	S102	2	273	165	0.27	0.65	0.29	1.41	1.04	6.52	4.81	4.63	3.11	4.14	1.05	0.02	0.17	0.09	0.05
19	S104	1	255	153	0.01	0.03	0.01	0.58	0.02	1.18	0.01	0.01	0.00	0.00	0.00	0.00	0.01	0.00	0.00
20	S104	2	236	153	0.00	0.01	0.00	0.01	0.01	0.04	0.03	0.02	0.02	0.04	0.02	0.00	0.00	0.00	0.00
				Total	19.87	39.48	19.46	41.25	36.19	109.32	48.59	59.24	27.00	43.93	27.34	2.99	8.34	0.93	3.56
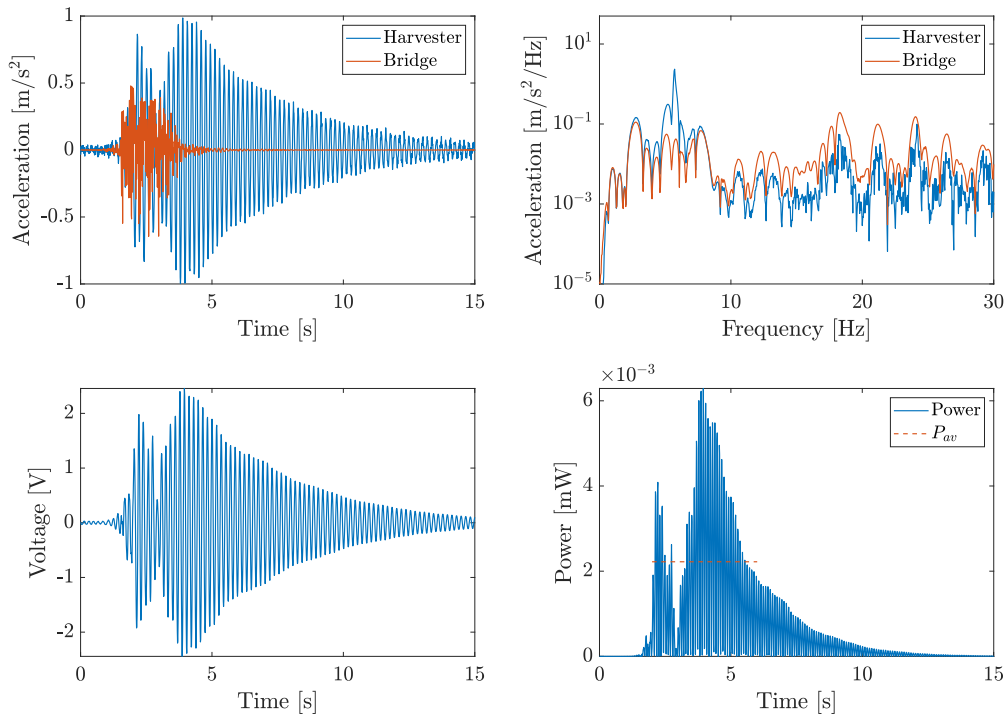
Fig. 17. Bridge and harvester acceleration, voltage and power at point A7 induced by Renfe S104 train circulating on track 2 at V = 251 km/h (passage #3).

5. Optimal design curves for railway bridges

This section presents optimal design curves for common railway bridges. Bridges of lengths from 12.5 m to 25 m in increments of 2.5 m were considered for the definition of optimal design curves. The fundamental frequencies for each span were selected from the band prescribed by Eurocode 1 (EC1) [37] for the application of simplified methods, as most existing bridges are expected to fall within these limits. Four evenly spaced sample values have been analysed between the lower and upper frequency limits (see Fig. 19). These frequencies are referred to as $f_{1,000}$, $f_{1,035}$, $f_{1,070}$ and $f_{1,100}$.

The material properties of the substructure were those of PLA identified in the previous section, the PZT properties coincide with the DuraAct patch transducer P-876.A12 [48] and the damping ratio was set at $\zeta = 0.69\%$. The optimal design curves represented
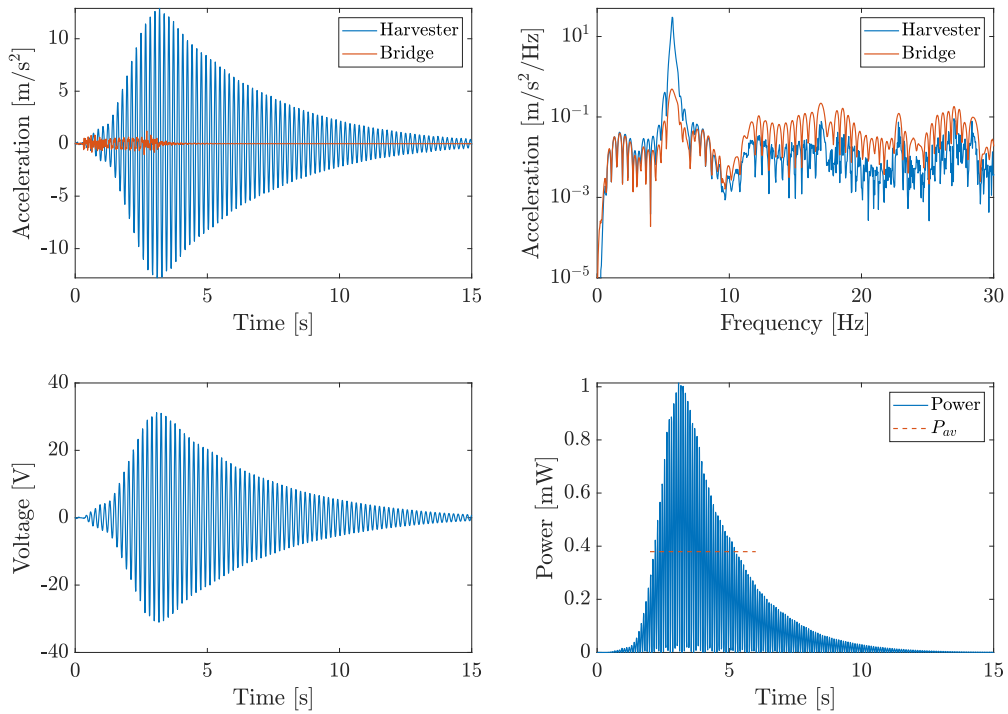
Fig. 18. Bridge and harvester acceleration, voltage and power at point $A7$ induced by Renfe S102 train circulating on track 2 at $V = 274\,km/h$ (passage #11).
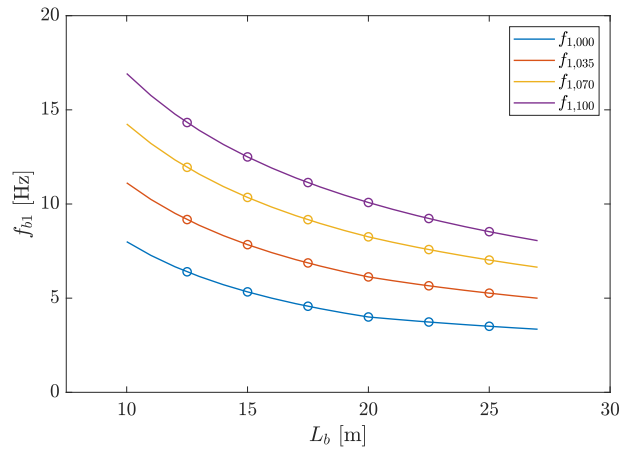

Fig. 19. Lower and upper frequency limits for simplified dynamic analysis of railway bridges [37].

in Fig. 20 define the thickness h_s and length L_s of the substructure, the tip mass M_t, and the load resistance R_l for the above mentioned bridges. The optimum harvester design for a bridge with length L_b and fundamental frequency f_{b1} is obtained once the design curve has been selected from Fig. 19. Then, the harvester properties are obtained from Fig. 20.

Figs. 19 and 20 show that the design parameters increase with the bridge span as the first natural frequency decreases. The design curve for the frequency band $f_{1,000}$ is especially significant since the optimal substructure length reaches the limit $L_{s,max} = 300\,mm$ for bridges with $L_b \geq 20\,m$. In these cases, the length of the substructure is constrained to $L_s = L_{s,max}$. The tuning device at low frequencies can be achieved by either increasing the mass or reducing the stiffness. An increase in mass produces higher stress levels in the substructure that may not comply with the integrity criteria defined in Section 2.4. Then, the proposed design curves for these bridges are obtained by reducing both the thickness and the mass to satisfy the integrity criterion, causing a drastic reduction in the output power (Fig. 21). Accounting for it, the design curves are valid for bridges with natural frequencies higher than $f_{b1} = 4.5\,Hz$.

The validity of the design curves is limited by the manufacturing process of the substructure and the properties of the PZT. The print settings of the specimens tested in Section 4.2 were common default parameters in most printing software. Therefore, the
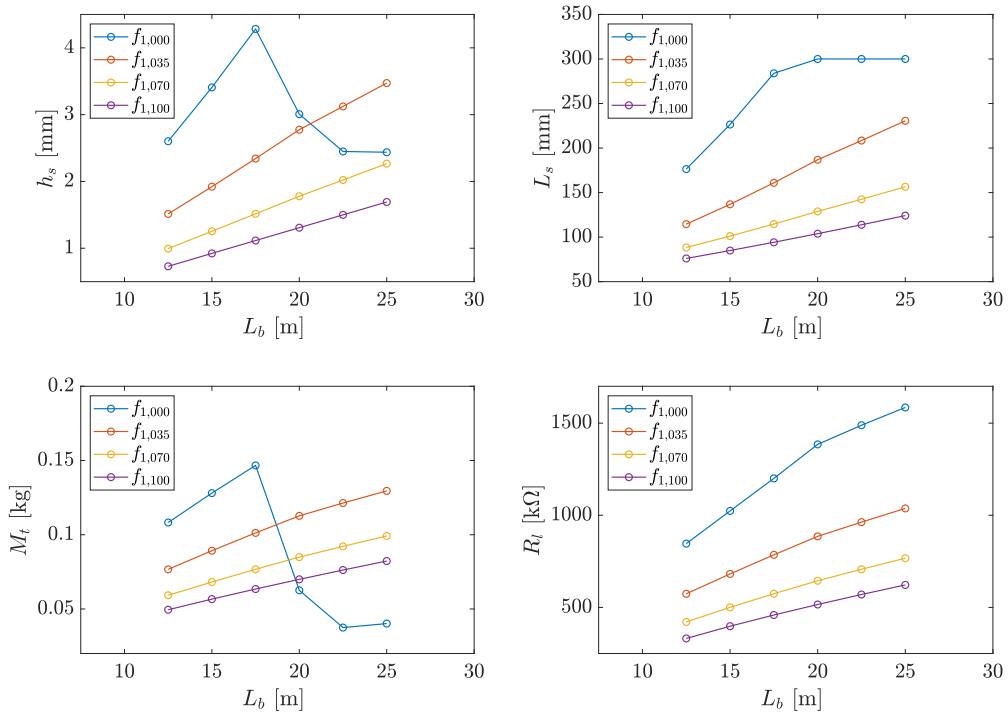
Fig. 20. Optimal design values of substructure thickness (h_s), substructure length (L_s), tip mass (M_t) and load resistance (R_l) for the bridges under study.
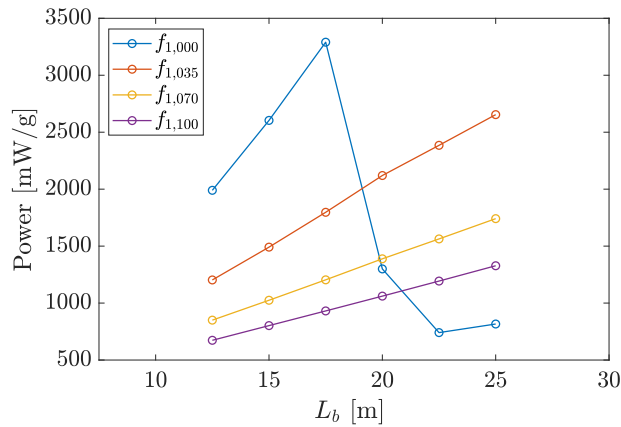

Fig. 21. Output power harvested for optimal design for bridges under study.

performance of the devices is expected to be close to the power estimated in Fig. 21. Any modification of the properties would require a new estimation of the optimal design following the tuning procedure in Section 2.4.

6. Conclusions

This research explored the design optimisation of energy harvesting devices for railway bridges using additive manufacturing. An analytical lumped-parameter model of the bimorph cantilever beam has been proposed to find the solution to the optimisation problem. The approach was derived from a variational formulation, considering the tip displacement as the generalised coordinate. The related dimensional shape function has been derived for bimorph cantilever beams with different PZT and substructure lengths. The governing equations are consistent with lumped-parameter models used in energy harvesting. The proposed solution agrees with distributed parameter solutions and FE models.

This research includes an experimental application of energy harvesting using acceleration data from a real bridge on the Madrid–Sevilla high speed line, over the Jabalón river. A prototype was designed and manufactured, and the PZT patch was the commercial

DuraAct patch transducer. Different 3D printing materials for the substructure were analysed. The study of material properties showed that the performance of the device increased with the material stiffness. PLA was selected for the substructure due to its low cost and ease of printing, making it one of the most widely used materials in 3D printing. In addition, PLA is a biodegradable and sustainable polymer made from organic sources.

The design was experimentally validated in the laboratory. The damping ratio of the system was found to be approximately 0.7%, which allowed a high rate of energy harvesting. The results show that the amount of energy harvested depends on the intensity of the rail traffic and the design of the harvester. The conclusions drawn from the experimental case study show that the energy in three and a half hours and 20 train passages could be 109.32 mJ. The amount of energy can be increased using several harvesters according to the output required power of a monitoring system. The energy could therefore be 471.67 mJ.

Finally, the optimal design curves for short- to medium-span railway bridges were estimated. The length and thickness of the substructure, the mass at the tip, and the resistance load increased with the bridge span as the first natural frequency decreased. The output power increased with the span of the bridge. The optimal design in bridges with fundamental frequencies below 4.5 Hz leads to long substructures that cannot be manufactured on most 3D printers. Although it is possible to limit the length of the substructure, the output power resulting from the optimal design drops significantly.

CRediT authorship contribution statement

J.C. Cámara-Molina: Conceptualization, Methodology, Software, Investigation, Validation, Writing – original draft, Writing – review & editing. **E. Moliner:** Conceptualization, Methodology, Software, Investigation, Validation, Writing – original draft, Writing – review & editing. **M.D. Martínez-Rodrigo:** Conceptualization, Methodology, Software, Investigation, Validation, Funding acquisition, Writing – original draft, Writing – review & editing. **D.P. Connolly:** Conceptualization, Methodology, Investigation, Supervision, Writing – original draft, Writing – review & editing. **D. Yurchenko:** Conceptualization, Methodology, Investigation, Supervision, Writing – original draft, Writing – review & editing. **P. Galvín:** Conceptualization, Methodology, Software, Investigation, Validation, Funding acquisition, Writing – original draft, Writing – review & editing. **A. Romero:** Conceptualization, Methodology, Software, Investigation, Validation, Funding acquisition, Supervision, Writing – original draft, Writing – review & editing.

Declaration of competing interest

The authors declare the following financial interests/personal relationships which may be considered as potential competing interests: Antonio Romero Ordonez reports financial support was provided by Spain Ministry of Science and Innovation. Antonio Romero Ordonez reports financial support was provided by Government of Andalusia Ministry of Economy Science Innovation and Employment.

Data availability

Data will be made available on request.

Acknowledgements

Appendix

The dimensionless shape function normalised to the tip displacement is:

$$\psi(x) = \frac{x^2(x - 3L_s)}{2L_s^3(\beta(\beta(\beta - 3) + 3)(\gamma - 1) - \gamma)}, \qquad 0 \le x \le L_p \qquad (A.1)$$

$$\psi(x) = \frac{\beta^2(2\beta - 3)(\gamma - 1)L_s^3 - 3\beta(\beta - 2)(\gamma - 1)L_s^2 x - 3\gamma L_s x^2 + \gamma x^3}{2L_s^3(\beta(\beta(\beta - 3) + 3)(\gamma - 1) - \gamma)}, \qquad L_p \le x \le L_s \qquad (A.2)$$

The equivalent mass and stiffness are:

$$M_{eq} = \left[\frac{\left(\begin{array}{c} \beta^5 \mu(5\beta(\beta - 7) + 63) - 35\beta^2(\beta - 1)(\beta(\beta - 3)(\beta(\beta - 3) + 6) + 12) - 33(\beta - 1)^7\gamma^2 + \\ 21\beta\gamma(\beta - 1)^4(3\beta(\beta - 3) + 11) \end{array} \right)}{(\gamma - \beta((\beta - 3)\beta + 3)(\gamma - 1))^2} \right] \frac{L_s \rho_s h_s b_s}{140} + M_t \qquad (A.3)$$

$$K_{eq} = \left[\frac{\gamma}{(\beta(\beta(3 - \beta) - 3)(\gamma - 1) + \gamma)} \right] \frac{3E_s I_s}{L_s^3} \qquad (A.4)$$

The effective mass is:

$$M_{eff} = L_s \rho_s h_s b_s \left[\frac{2\beta(\beta-1)(\beta(\beta-3)+6) - 3\gamma(\beta-1)^4 + \mu\beta^3(\beta-4)}{8\beta(\beta(\beta-3)+3)(\gamma-1) - 8\gamma} \right] + M_t \tag{A.5}$$

The electromechanical coupling coefficient is:

$$\alpha = \left[\frac{3\beta(\beta-2)}{2L_s(\beta(\beta(\beta-3)+3)(\gamma-1)-\gamma)} \right] e_{31} h_{pc} b_p \tag{A.6}$$

The parameters β, γ and μ relating the length, bending stiffness, and mass of the beam section with PZT to the substructure are given by Eq. (1).

References

[1] G. De Roeck, The state-of-the-art of damage detection by vibration monitoring: The SIMCES experience, J. Struct. Control. 10 (2) (2003) 127–134.
[2] D. Barke, K.W. Chiu, Structural health monitoring in the railway industry: A review, Struct. Health Monit. 4 (1) (2005) 81–94.
[3] M. Vagnoli, R. Remenyte-Prescott, J. Andrews, Railway bridge structural health monitoring and fault detection: State-of-the-art methods and future challenges, Struct. Health Monit. 17 (4) (2018) 971–1007.
[4] C. Wei, X. Jing, A comprehensive review on vibration energy harvesting: Modelling and realization, Renew. Sustain. Energy Rev. 74 (2017) 1–18.
[5] T. Yildirim, M.H. Ghayesh, W. Li, G. Alici, A review on performance enhancement techniques for ambient vibration energy harvesters, Renew. Sustain. Energy Rev. 71 (2017) 435–449.
[6] M.R. Sarker, S. Julai, M.F.M. Sabri, S.M. Said, M.M. Islam, M. Tahir, Review of piezoelectric energy harvesting system and application of optimization techniques to enhance the performance of the harvesting system, Sensors Actuators A 300 (2019).
[7] M. Peigney, D. Siegert, Piezoelectric energy harvesting from traffic-induced bridge vibrations, Smart Mater. Struct. 22 (9) (2013).
[8] T. McEvoy, E. Dierks, J. Weaver, S. Inamdar, K. Zimowski, K.L. Wood, R.H. Crawford, D. Jensen, Developing innovative energy harvesting approaches for infrastructure health monitoring systems, in: Proceedings of the ASME Design Engineering Technical Conference 5, (PARTS A and B), 2011, pp. 325–339.
[9] J.J. Wang, G.P. Penamalli, L. Zuo, Electromagnetic energy harvesting from train induced railway track vibrations, in: Proceedings of 2012 8th IEEE/ASME International Conference on Mechatronic and Embedded Systems and Applications, MESA 2012, 2012, pp. 29–34.
[10] Y. Tianchen, Y. Jian, S. Ruigang, L. Xiaowei, Vibration energy harvesting system for railroad safety based on running vehicles, Smart Mater. Struct. 23 (12) (2014).
[11] A. Pourghodrat, C.A. Nelson, S.E. Hansen, V. Kamarajugadda, S.R. Platt, Power harvesting systems design for railroad safety, Proc. Inst. Mech. Eng. F 228 (5) (2014) 504–521.
[12] P. Cahill, N.A.N. Nuallain, N. Jackson, A. Mathewson, R. Karoumi, V. Pakrashi, Energy harvesting from train-induced response in bridges, J. Bridge Eng. 19 (9) (2014).
[13] F.U. Khan, I. Ahmad, Review of energy harvesters utilizing bridge vibrations, Shock Vib. 2016 (2016).
[14] Y. Song, Finite-element implementation of piezoelectric energy harvesting system from vibrations of railway bridge, J. Energy Eng. 145 (2) (2019).
[15] A. Erturk, D.J. Inman, Broadband piezoelectric power generation on high-energy orbits of the bistable Duffing oscillator with electromechanical coupling, J. Sound Vib. 330 (10) (2011) 2339–2353.
[16] P. Museros, E. Alarcón, Influence of the second bending mode on the response of high-speed bridges at resonance, J. Struct. Eng. 131 (3) (2005) 405–415.
[17] P. Galvín, A. Romero, E. Moliner, M.D. Martínez-Rodrigo, Two FE models to analyse the dynamic response of short span simply-supported oblique high-speed railway bridges: Comparison and experimental validation, Eng. Struct. 167 (2018) 48–64.
[18] A. Romero, J.C. Cámara-Molina, E. Moliner, P. Galvín, M.D. Martínez-Rodrigo, Energy harvesting analysis in railway bridges: An approach based on modal decomposition, Mech. Syst. Signal Process. 160 (2021).
[19] N. Stephen, On energy harvesting from ambient vibration, J. Sound Vib. 293 (1) (2006) 409–425.
[20] C.D. Richards, M.J. Anderson, D.F. Bahr, R.F. Richards, Efficiency of energy conversion for devices containing a piezoelectric component, J. Micromech. Microeng. 14 (5) (2004) 717–721.
[21] J. Xu, J. Tang, Linear stiffness compensation using magnetic effect to improve electro-mechanical coupling for piezoelectric energy harvesting, Sensors Actuators A 235 (2015) 80–94.
[22] T.C. De Godoy, M.A. Trindade, J.F. Deü, Topological optimization of piezoelectric energy harvesting devices for improved electromechanical efficiency and frequency range, in: 10th World Congress on Computational Mechanics, 2014, pp. 4003–4016.
[23] S. Nabavi, L. Zhang, Mems piezoelectric energy harvester design and optimization based on genetic algorithm, in: IEEE International Ultrasonics Symposium, IUS 2016-November, 2016.
[24] A. Kumar, A. Sharma, R. Kumar, R. Vaish, V.S. Chauhan, Finite element analysis of vibration energy harvesting using lead-free piezoelectric materials: A comparative study, J. Asian Ceram. Soc. 2 (2) (2014) 138–143.
[25] R. Mohamed, M.R. Sarker, A. Mohamed, An optimization of rectangular shape piezoelectric energy harvesting cantilever beam for micro devices, Int. J. Appl. Electromagn. Mech. 50 (4) (2016) 537–548.
[26] M.R. Sarker, A. Mohamed, R. Mohamed, A new method for a piezoelectric energy harvesting system using a backtracking search algorithm-based PI voltage controller, Micromachines 7 (10) (2016).
[27] M.R. Sarker, A. Mohamed, R. Mohamed, Improved proportional-integral voltage controller for a piezoelectric energy harvesting system converter utilizing lightning search algorithm, Ferroelectrics 514 (1) (2017) 123–145.
[28] P. Peralta, R. Ruiz, S. Natarajan, E. E Atroshchenko, Parametric study and shape optimization of piezoelectric energy harvesters by isogeometric analysis and kriging metamodeling, J. Sound Vib. 484 (2020).
[29] D. Yurchenko, L.Q. Machado, J. Wang, C. Bowen, S. Sharkh M. Moshrefi-Torbati, D.V. Val, Global optimisation approach for designing high-efficiency piezoelectric beam-based energy harvesting devices, Nano Energy 93 (2022).
[30] L.L. López Taborda, H. Maury, J. Pacheco, Design for additive manufacturing: A comprehensive review of the tendencies and limitations of methodologies, Rapid Prototyp. J. 27 (5) (2021) 918–966.
[31] C. Chen, X. Wang, Y. Wang, D. Yang, F. Yao, W. Zhang, B. Wang, G.A. Sewvandi, D. Yang, D. Hu, Additive manufacturing of piezoelectric materials, Adv. Funct. Mater. 30 (52) (2020).
[32] J.-I. Park, G.-Y. Lee, J. Yang, C.-S. Kim, S.-H. Ahn, Flexible ceramic-elastomer composite piezoelectric energy harvester fabricated by additive manufacturing, J. Compos. Mater. 50 (12) (2016) 1573–1579.
[33] Z. Chen, X. Song, L. Lei, X. Chen, C. Fei, C.T. Chiu, X. Qian, T. Ma, Y. Yang, K. Shung, Y. Chen, Q. Zhou, 3D printing of piezoelectric element for energy focusing and ultrasonic sensing, Nano Energy 27 (2016) 78–86.
[34] Y. Zeng, L. Jiang, Y. Sun, Y. Yang, Y. Quan, S. Wei, G. Lu, R. Li, J. Rong, Y. Chen, Q. Zhou, 3D-printing piezoelectric composite with honeycomb structure for ultrasonic devices, Micromachines 11 (8) (2020).

[35] S. Gowthaman, G.S. Chidambaram, D.B.G. Rao, H.V. Subramya, U. Chandrasekhar, A review on energy harvesting using 3D printed fabrics for wearable electronics, J. Inst. Eng. India Ser. C 99 (4) (2018) 435–447.

[36] G.A.F. Seber, C.J. Wild, Nonlinear Regression, Wiley-Interscience, Hoboken, NJ, 2003.

[37] CEN, EN 1991-2, Eurocode 1: Actions on Structures - Part 2: Traffic loads on bridges, European Committee for Standardization, Brussels, 2002.

[38] IEEE Standard on Piezoelectricity, Standard, 1998.

[39] A. Erturk, D.J. Inman, An experimentally validated bimorph cantilever model for piezoelectric energy harvesting from base excitations, Smart Mater. Struct. 18 (2) (2009).

[40] A. Erturk, D.J. Inman, Parameter identification and optimization in piezoelectric energy harvesting: Analytical relations, asymptotic analyses, and experimental validations, Proc. Inst. Mech. Eng. I 225 (4) (2011) 485–496.

[41] P. Galvín, A. Romero, E. Moliner, D.P. Connolly, M.D. Martínez-Rodrigo, Fast simulation of railway bridge dynamics accounting for soil–structure interaction, Bull. Earthq. Eng. (2021).

[42] Materials Technical Data (Typical Values), https://info.piezo.com/hubfs/Data-Sheets/piezo-material-properties-data-sheet-20201112.pdf.

[43] Ansys Academic Research Mechanical, Release 2022 R1, Help System, Coupled Field Analysis Guide, ANSYS, Inc.

[44] M. Zhu, E. Worthington, J. Njuguna, Analyses of power output of piezoelectric energy-harvesting devices directly connected to a load resistor using a coupled piezoelectric-circuit finite element method, IEEE Trans. Ultrason. Ferroelectr. Freq. Control 56 (7) (2009) 1309–1318.

[45] J. Park, S. Lee, B.M. Kwak, Design optimization of piezoelectric energy harvester subject to tip excitation, J. Mech. Sci. Technol. 26 (1) (2012) 137–143.

[46] P. Galví, A. Romero, E. Moliner, G. De Roeck, M.D. Martínez-Rodrigo, On the dynamic characterisation of railway bridges through experimental testing, Eng. Struct. 226 (2020).

[47] E. Reynders, System identification methods for (operational) modal analysis: Review and comparison, Arch. Comput. Methods Eng. 19 (1) (2012) 51–124.

[48] P-876 DuraAct Patch Transducer information, https://www.piceramic.com/en/products/piezoceramic-actuators/patch-transducers/p-876-duraact-patch-transducer-101790/.

[49] Ultrafuse filamnets, https://www.ultrafusefff.com.

[50] MCPP 3D filaments, https://mcpp-3dp.com.

[51] ASTM Designation: D638—14 Standard Test Method for Tensile Properties of Plastics, 2014.

[52] Deutsches Institut für Normung, DIN 45672 Teil 2: Schwingungsmessungen in der Umgebung von Schienenverkehrswegen: Auswerteverfahren, 1995.